AERODYNAMIC PERFORMANCE ENHANCEMENT OF A NACA 66-206 AIRFOIL USING SUPERSONIC CHANNEL AIRFOIL DESIGN

A Thesis

presented to

the Faculty of California Polytechnic State University,

San Luis Obispo

In Partial Fulfillment

of the Requirements for the Degree

Master of Science in Aerospace Engineering

By

David Michael Giles

September 2009

COMMITTEE MEMBERSHIP

TITLE:	Aerodynamic Performance Enhancement of a NACA 66-206 Airfoil Using Supersonic Channel Airfoil Design
AUTHOR:	David Michael Giles
DATE SUBMITTED:	September 2009
COMMITTEE CHAIR:	Dr. David D. Marshall, Associate Professor
COMMITTEE MEMBER:	Dr. Jin Tso, Professor
COMMITTEE MEMBER:	Dr. Eric A. Mehiel, Assistant Professor
COMMITTEE MEMBER:	Dr. Peter J. Schuster, Associate Professor

ABSTRACT

Aerodynamic Performance Enhancement of a NACA 66-206 Airfoil Using Supersonic Channel Airfoil Design

David Michael Giles

Supersonic channel airfoil design techniques have been shown to significantly reduce drag in high-speed flows over diamond shaped airfoils by Ruffin and colleagues. The effect of applying these techniques to a NACA 66-206 airfoil is presented. The design domain entails channel heights of 8-16.6% thickness-to-chord and speeds from Mach 1.5-3.0. Numerical simulations show an increase in the lift-to-drag ratio for airfoils at Mach 2.5 at a 35,000-ft altitude with a 12% channel height geometry showing a benefit of 17.2% at 6-deg angle of attack and a sharp channel leading edge. Wave drag is significantly reduced while viscous forces are slightly increased because of greater wetted area. Lift forces compared to clean airfoil solutions were also decreased, due mainly to the reduction in the length of the lifting surfaces. A tensile yield failure structural analysis of a typical beam found an 11.4% channel height could be implemented over 50% of the span between two typical ribs. A three dimensional wing was designed with the determined slot geometry and two dimensional flow analyses. An overall increase in L/D of 9% was realized at Mach 2.5 at a 35,000-ft altitude and 6-deg angle of attack.

TABLE OF CONTENTS

Page

LIST OF TABLES

Page

LIST OF FIGURES

Page

Page

Page

CHAPTER 1

Introduction and Review of Literature

Tailoring the aerodynamic performance of a high speed aircraft such as a supersonic civil transport towards cruise conditions can optimize criteria such as range, fuel fraction, and payload. By optimizing these, a cheaper cost per seat per flight mile can be achieved for a transport aircraft and more profit can be made. By maximizing L/D many of these performance parameters can be improved. However, to reach supersonic speeds, a self-propelled aircraft must traverse both the subsonic and transonic regimes. Many airfoils designed only for supersonic cruise performance, such as a diamond airfoil, have very low lifting characteristics at slow speeds. To counteract this, in some wing designs cambered airfoils are used in some sections to provide lift for subsonic operation. In supersonic flight, this cambered and often blunted nose airfoil section has a lower L/D because of the high wave drag associated with the stagnation point, hindering the cruise performance of the aircraft. By improving the L/D for a cambered airfoil during supersonic flight, the penalty of designing some of the lifting surfaces for the subsonic regime can be reduced.

This thesis examines the supersonic performance of a NACA 66-206 airfoil. The 6 series airfoil family was developed by NACA to obtain desirable drag, critical Mach number, and also maximum lift characteristics (Abbot pg.120). This particular airfoil exhibits characteristics akin to that of a typical supercritical airfoil including a flat topped portion of the airfoil to delay the formation of a shock on the top surface and also a cusped section along the bottom surface near the trailing edge to promote lift in the subsonic regime (Anderson pg.539). The analysis will consist of three portions. First, a

two dimensional aerodynamic analysis of the airfoil will be conducted to determine the L/D performance of an infinite span wing. Next a structural analysis will be performed on a typical spar. The structural integrity of the spar determines how much the airfoil can be modified. Finally, the initial aerodynamic and structural results will be analyzed to find a three dimensional design solution upon which an aerodynamic flow field model will be analyzed.

To improve the supersonic aerodynamic performance of the wing, an interior channel will be implemented from the leading edge to the trailing edge of the airfoil. By doing this, the pressure drag on the airfoil will decrease more than that of the increase in viscous drag due to the increase in wetted area. This overall reduction in drag will allow the lift to drag ratio to increase when compared to the original airfoil, improving the performance of the profile. The structural analysis portion will show that a typical spar can be modified by cutting out a hole in the web of the spar. This design will determine how large the channel can be to pass through the wing without adding additional structural weight to the spar when the tensile yield stress failure criterion is used. In the 3D aerodynamic analysis, the combination of both the 2D aerodynamic models and the structural models will show a design that contains no additional structural weight but allows for an increase in L/D performance. The geometry analyzed will show that the complex interaction of a channel airfoil and a baseline airfoil profile will not be detrimental to the performance enhancement seen in the two dimensional results when the two profiles are both present on a wing.

The aerodynamic analysis will be over a range of Mach numbers to determine where the best benefit of using this type of technology will obtained. The improvement

will be examined from a freestream Mach number of 1.5 to 3. The subsonic and transonic regimes will not be studied because it is assumed that the channel will be opened after cruise conditions have been reached. A cruise altitude of 35,000 ft with standard atmospheric properties was chosen. The channel heights to be tested will range from 8% of the maximum airfoil thickness to 16.6%. Also different types of leading edges for the channel will be assessed to determine the effect of rounded leading edges as opposed to sharp ones. An angle of attack of 6° will be introduced to obtain a significant amount lift to accurately examine the L/D performance for different channels and Mach numbers. The structural portion will look at a representative section of the wing. The main goal of the structural analysis is to determine a basic framework for the feasibility of this enhancement when other disciplines are taken into account. Because of this approach, the failure criterion will be for the tensile yield stress limit. Other criteria may be more constraining but it can be more difficult to obtain accurate results. The three dimensional aerodynamic analysis will look at one design condition obtained by comparing both the structural and aerodynamic results. As in the structural analysis, this analysis will observe a basic design and the penalties that occur when a finite three dimensional model is used. Wing sweep will not be examined in order to create accurate symmetry planes.

An airfoil section during supersonic flight experiences drag in three categories: skin friction drag, induced drag, and wave drag. The wave drag is the drag from the airfoil's thickness and the bluntness of both the leading and trailing edges of the section. This drag is calculated as part of the pressure drag component. The skin friction drag is caused by the viscosity of the air and is measured as the viscous component of drag.

Previous solutions to reduce the supersonic drag on a wing, fin, or tail were to use a sharp diamond airfoil. However, the very sharp edges inherent to a sharp diamond airfoil design are not very practical. A sharp leading edge is both difficult and expensive to manufacture. Also, in order to have some structural strength, some blunting is required. This is seen on many airfoils which have a "sharp" trailing edge. Also, a sharp leading edge is not conducive to keeping the flow attached at angles of attack. Lastly, at high Mach numbers, the heat transfer of a sharp leading edge can be high enough to melt the structure. This study does not deal with Mach numbers of that nature.

A typical airfoil used at non-cruise conditions such as takeoff, landing, and climbing have a blunted leading edge in order to prevent flow separation at angle of attack, a condition which is characteristic to a sharp leading edge airfoil. The disadvantage of this blunting is that at supersonic cruise, the sharp leading edge airfoil will experience lower drag than that of the blunted airfoil.

Previous designs attempted to combine the advantages of the blunted and sharp leading edge airfoils by creating a blunted diamond shaped airfoil. This airfoil had drag performance that was between the sharp diamond airfoil and a typical rounded leading edge airfoil. In order to decrease the drag further, Ruffin (Ruffin, AIAA 2000) amended the design of the blunted diamond shape airfoil. To reduce the pressure drag, a hollow channel through the airfoil section was developed. This channel would only open during supersonic cruise, preserving the performance of the airfoil at off-design conditions. When the baseline no-channel airfoil is used, the pressure acting on the leading edge in the stagnation region is high. Most of the drag on the airfoil is located here. When the channel is implemented, the surface that experienced this high pressure region is

eliminated and the high pressure region is dispersed to either side of the channel. From this elimination, the wave drag of the airfoil is decreased.

With the channel geometry, the wetted area of the airfoil is increased. Using CFD techniques, Ruffin (Ruffin, AIAA 2000) found that the decrease in wave drag far exceeded the increase in viscous drag, lowering the total drag by about 20% for fully turbulent models. From a no-channel geometry to a sharp leading edges channeled geometry the wave drag decrease was 55 counts whereas the viscous drag only increased by about 30 counts for an overall decrease from 205 counts to 180. This data was from the design condition of Mach 2.4 flow at a zero-lifting condition and a low altitude of 12 km.

The study also looked at different types of internal channel geometries. Because of the symmetry of the blunted diamond airfoil, the channel midline ran straight from the leading edge, to the trailing edge. Two wall geometries were looked at; one with a straight wall parallel to the midline and also a geometry where the walls diverged at a 0.1° half angle. With the straight channels, the flow inside the channel was maintained at subsonic speeds the whole way. The choke point occurs near the trailing edge. Since the boundary layer grew as the flow traveled down the channel, the flow choked at the point where the inviscid flow down the center of the channel was at the narrowest point. The diverging channel choked at the leading edge and supersonic flow was present for the remainder of the channel. The supersonic flow in the channel gave a higher amount of viscous drag because of the greater speed in the channel. In comparable airfoils, the increase in drag was about 18%. However, the direction of the pressure forces acting on the walls of the channel gave a slight propulsive force. This gave a lower pressure drag of

about 15%. Since the overall pressure drag was much higher in magnitude, the overall drag decreased by about 6%. The current study of the NACA 66-206 airfoil, a 0.05° half angle was used to obtain some propulsive force while trying to keep the interior flow as subsonic as possible.

The height of the channel also determines the flow field and the drag characteristics of the airfoil. In the same study by Ruffin, the channel height was varied from 0.004c to 0.016c. as the channel size increased so did the decrease in drag. For a laminar flow solution, the decrease went from 33% to a 78% reduction inn the drag coefficient. For the smaller 0.004c channel, the "choked-channel" condition existed. This was where the channel was sufficiently small that the flow is choked at the channel entrance and enters the channel at subsonic speeds. This condition causes a leading edge bow shock, similar to that of the baseline airfoil. For larger channels, the flow was not choked and a flowfield identical to that of a started supersonic inlet was produced. In this case, the flow enters the channel supersonically. The main difference in these cases was heat transfer, which was not specifically examined in this thesis. For hypersonic flows, heat transfer to the airfoil is critical to maintaining the structure. The started inlet conditions had much higher heat transfer rates than the bow shock condition and were present on the channels with a larger height. However, at lower supersonic speeds, the heat transfer rate is lower, even if the inlet has a started condition. Depending on the application required for the channel inlet design, having a larger channel to reduce the drag further but introducing a started inlet condition may be acceptable, especially at the slower supersonic speeds.

Another study was performed to optimize the leading edge lips of the blunted diamond airfoil shape for aerothermodynamic performance. Gupta and Ruffin (Gupta, 1999) analyzed various channel heights, nose radii for both the blunted diamond airfoil and the channel lips, and also different interior channel geometries at a high Mach number of four. The optimal airfoil contained a diverging interior channel and a rounded nose lip radius of 0.00272c. In this study, the size of the airfoil was allowed to change in order to keep the same enclosed volume as the baseline airfoil. Even when the airfoil was thicker and had a greater wetted surface area because of the increased length, the drag was still less than that of the baseline airfoil. The scaling was introduced to take into account structural considerations such as fuel volume and to leave as much space within the wing as was available before the airfoil modification. By doing this, the overall airfoil shape was changed from the baseline so a simple opening of a channel was no longer possible. Also, analysis of the interior structure would not be an accurate comparison of similar structures if the chord length would grow from the baseline to the optimized airfoil when the channel was opened. A response surface was generated to predict lift and drag for the various alterations in the geometry. For the optimal airfoil, the predictions were only off by 4% for only 28 total data points for six variables.

In both studies, angle of attack was introduced in order for the section to produce lift. Angles of up to 25° were used (Gupta, 2000). The introduction of the channel lowered the drag at all angles of attack. For the blunted diamond airfoil shape, the lift produced was not affected by the implementation of the channel. When the channel was carved out of the blunted airfoil, the chord length remained basically unchanged causing a similar amount of external lifting surface to remain. The flow going into the channel

had no adverse effect on lift since the pressure was equal on both upper and lower surfaces of the channel. Since the overall drag was decreased and the lift unchanged, the L/D was increased with a maximum of performance improvement of 20% for fully turbulent flow.

The performance of the supersonic channel airfoil design was also extended to three dimensional objects (Gupta, 2000). The main application examined was a sphere-cone to test the concept on a three dimensional body such as a reentering spacecraft. At an angle of attack of 5°, the drag only decreased about 3.6%, but much better lift performance was seen. The increase of 20.6% in the lift coefficient provided an overall performance improvement of 25.1% for L/D. In a zero lift condition, the sphere cone geometry had similar performance characteristics as the two dimensional flow when geometric parameters were changed. The larger the channel implemented, the greater the drag reduction observed with a maximum decrease of nearly 20% for a Navier-Stokes solution to a channel of 16% of the base diameter of the cone. These experiments were observed at Mach 7.

Experimental correlation of the predicted performance improvement was also examined for Mach 2-2.5 flow for the three dimensional model. In the wind tunnel test, the experimental model found a drag reduction of 9.2% for the channel case compared to the baseline. The computer models only predicted an 8.4% decrease. The discrepancy could be attributed to the turbulence model and the difficulty in predicting separation regions at the trailing end of the sphere-cone base.

For the 3D axisymmetric body, variations in the channel design were examined. The baseline geometry was a blunted cylinder with a conical flared afterbody (Gupta,

2000). The straight channel geometry again provided an overall drag reduction of 3.9%. A cowl-like geometry, where the channel begins at the leading edge of the body and exits along the external surface of the cylinder portion of the body, provided a decrease of 5.7% when compared to the baseline. Less benefit was seen for the cowl geometry for pressure drag, but because of the shorter channel and smaller wetted area, the viscous drag of the cowl geometry was less than the straight channel body. The viscous effects outweighed the pressure drag to create the slightly higher performance. Another benefit of the cowl channel was the location of the channel. Since it was only near the leading edge, much of the interior structure can remain intact and bulkier payloads may be possible. A straight channel geometry has a large hole throughout the entire body which could limit the payloads that can be transported.

There are a few key differences between previous research, and the analysis performed for the current research. Previous airfoils have been of a symmetric design. However, at subsonic speeds, higher angles of attack are needed in order to create enough lift as opposed to a non-symmetrical airfoil. In many situations, these non-symmetrical airfoils are needed to provide the lift to allow the aircraft to reach supersonic cruise condition. The current study will try to examine an airfoil that was not specifically designed for supersonic cruise and try to improve its performance during that portion of flight. Also the structural implementation when dealing with actual flight loads and interior structure has not been specifically examined. This study will expand on that to see the feasibility of altering the airfoil. Lastly, the interaction of a channeled airfoil section and a non channeled section and how the airfoils connect when placed on a wing

will be examined. The attachment zones are an area which has yet to be explored when using a supersonic channel airfoil design.

CHAPTER 2

Methods

2D Airfoil Analysis

Initially it was desired to use a supercritical type airfoil and improve its performance in the supersonic range by implementing the channel design. Two airfoils were subject to initial studies. The NASA SC20712 and SC20714 airfoils were examined. However, because of the difficulty in shaping the outlet of the channel because of the large cusp these airfoils were not used. The baseline airfoil selected for this exploration was a NACA 66-206 airfoil, a 6% thick airfoil, as seen in Figure 1. The coordinates describing the airfoil were obtained from the UIUC airfoil database (UIUC, 2007) which described the airfoil by 50 points. The airfoil was chosen because it was similar to that of the inboard airfoil on the reference supersonic transport airplane (Rinioe, 2004). The reference aircraft also used a 66 series, but it was 3% thick airfoil. The change to a 6% thick airfoil was done because of the greater availability of general aerodynamic data than the 3% thick airfoil (Abbot pg.656).

Figure 1. NACA 66-206 Airfoil

The airfoil coordinates were then imported into the computer aided drafting (CAD) program Solidworks. The coordinates were input as a spline and were broken at the trailing edge of the airfoil. This allowed a sharp trailing edge to be created and the leading edge was set as a continuous part of the spline. This was important because if the spline was broken at the leading edge then a wedge type geometry would be imported. This would cause the shock to be attached instead of causing a bow shock when the airfoil was placed in the supersonic flowfield which was not desired.

After the raw airfoil coordinates had been imported into the CAD program, it was then exported as a parasolid model with extension .X_T. The parasolid was then imported into the meshing program Gambit. Here the flowfield was meshed appropriately. The finalized mesh was exported as a 2-D mesh and read into the flow solver program Fluent. The Fluent program was run on Linux OS generic PCs with dual core capability. The dual cores allowed Fluent to take advantage of its parallel computing ability to allow for faster run times.

Naming Conventions

In order to keep track of the different channel airfoil configurations, a simple naming convention was created as seen in Figure 2. The first letter determines what baseline airfoil was used. A “c” designation denotes the NACA 66-206 airfoil. The second letter and first number show what how round the leading edge is. “r6” describes a 0.006c diameter rounding of the leading edge or lip of the channel whereas “r0” would mean a sharp leading edge for the lips. The next combination describes the channel height. The channel heights ranged from 8% to 16.6% of the thickness to chord ratio. The

next descriptor shows the freestream Mach number of the case. Finally, the last grouping tells the angle of attack the airfoil is experiencing.

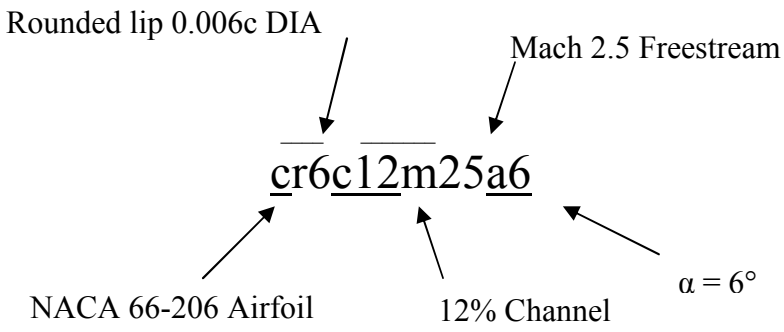

Figure 2. Example of Naming Convention Used

CFD Solver

In order to obtain a solution to the flowfield, a progression of models were needed. Because of the expansion waves, shocks, and fluid compressibility, if the system used the full turbulence model, the solver would diverge and a solution could not be found. To compensate for this, the flowfield can be solved for on a general level and then further refined to reach a more accurate solution.

The first model used was the laminar model. In a laminar model, the flowfield has parallel streamlines that do not intersect. Laminar models are most accurate at low Reynolds numbers less than about 2000. This is much lower than the Reynolds number for the supersonic flows examined in this study. However, the laminar model is much simpler to compute and can give a general idea of the flowfield characteristics without using an expensive turbulence model calculation. By using the laminar model, the shock

and expansion wave locations can be determined before implementing the more complex calculations of the turbulent models to determine overall lift and drag.

Two turbulent models were used to determine the lift and drag on the NACA 66-206. The first model used was a 2-equation model, the standard k-ε where k is the turbulent kinetic energy and ε is the dissipation rate. This is a semi-empirical model that uses constants determined from air and water experiments (FLUENT, Tannehill). The model assumes that the flow is fully turbulent. This model was used initially as it is the basic 2-equation model for CFD analysis. The introduction of the viscous terms adds considerable computation time but provides a more accurate determination of the location of the flow field features and prediction of the lift and drag on the airfoil.

Additional models have been developed based on the initial k-ε model to improve the prediction. The model used in this research was the k-ω model with shear stress transport (SST). The k-ω model uses the k-ε model for the high Reynolds number parts of the flow field. This includes most of the flow field that is not in the boundary layer. The k-ω portion is applied in the boundary layer. The SST variation of the k-ω model is used because it allows for a more gradual change from where the two models are used. For this research, the flow field was initially solved with the k-ε model to determine the flow field characteristics with the viscous effect included. The second turbulence model was then used to provide additional accuracy in the prediction.

An important parameter to consider in turbulence modeling is inner variable y^+. This variable is a non-dimensional relationship of the distance from the wall, fluid viscosity, and wall shear. This allows any boundary layer to be expressed by a non-dimensional term despite speed or boundary thickness. The boundary has three zones as

described by the y^+ value. For y^+ less than 5, this is considered the viscous sublayer where the no slip condition is present. The boundary layer is linear in this section. From 5 to 30, the buffer zone exists which is a transition layer. From 30 to 300 or more, the logarithmic region exists. In CFD, the y^+ is important because if the node value is less than 30, wall functions cannot be used. If the closest node to the body has a value of 300 or more, an accurate determination of the viscous effects due to the boundary layer is not feasible.

A method to determine accurate representation of the flow field while saving computation time is grid adaptation. A coarse grid is initially solved for in order to determine the approximate location of the major flow features such as bow shocks and expansion waves. Once the flow features have been established, the grid is examined for the regions with the highest change, or gradient, between cells for a certain parameter. Parameters can include density, temperature, or pressure, which was the gradient selected in this study as the pressure difference across a shock is very high. Once the regions are identified, the grid is refined by splitting the cell in to four smaller cells. Usually a limit on the gradient from cell to cell is chosen so many cells are adapted per iteration. After the flow field has been solved using the new refined grid, the overall flow field is examined and the grid can either be coarsened (four cells merge into one cell) if the gradient is very low or again refined. This save computation time by allowing the cell size to be small in only the critical areas and in non-critical areas the cell size can be larger making the computation cheaper for that portion. A second grid adaptation used in this study was for y^+. A hard limit of less than 100 and greater than 30 was set. The

boundary cells were refined and coarsened to meet this criteria as the boundary layer flow field was determined through the many iterations of the solver.

Another technique to reduce computation time is multi-gridding. With very fine grids it often takes a large amount of computation time to propagate the boundary conditions through out the whole mesh. The multi-grid uses several mesh levels to coarsen the grid in order to decrease time to convergence. In a simple study, the use of 1 multi-grid level decreased the conversion by a factor of 1/13 (Tannehill). Multiple levels give diminishing returns. A secondary benefit is that is removes low-frequency computational errors that can be present on fine grids by examining the mesh at a coarser stage where the low frequency errors become high frequency. The multi grid technique takes the current mesh (level 1) and coarsens it through multiple levels. The residual value for each grid point is propagated up to the next level (level 2) which has a grid that is about half the number of cells. The residuals are then calculated again and projected onto a further coarsened grid (level 3). This continues up to the number of levels desired. For this study, the multi-grid was used to four levels and was used for the three dimensional case only to speed up the large computation time for each 3D iteration.

Baseline Airfoil Model Generation

The baseline airfoil was input simply by importing the points and generating a spline around them as described at the beginning of this chapter.

Channel Airfoil Model Generation

The generation of the channel airfoil started with the imported baseline airfoil. This airfoil was then modified in order to have the same starting point for comparative

purposes after the flow field had been solved. The channel was split into three major areas that modified the original airfoil.

The first section modified was the leading edge inlet to the channel. Initially, all airfoils had rounded leading edges. The center of the channel inlet was aligned with the furthermost leading point of the airfoil. Next the top part of the airfoil was rounded off. For each rounded case, the diameter of the top lip at the leading edge was 0.006c. This was chosen because it was the optimum height from previous research (Gupta, 1999). The rounding location was determined by making the circular cut be tangent both to the airfoil and the horizontal channel. Depending on the size of the channel, the new leading edge was located closer or further from the original leading edge: 0.0114c and 0.0226c for the 8% and 16.6% channels respectively. Because of the asymmetric nature of the baseline airfoil, the lower lip was not the same shape as the upper lip of the channel. In order to maintain the general shape of the baseline airfoil, the lower lip was not modified with the 0.006c diameter rounding. Instead, the circular rounding was applied similarly as before but with three tangential requirements: the baseline airfoil, the horizontal channel, and the leading edge of the upper lip. A sample of what the geometry of a rounded leading edge airfoil can be seen in Figure 3.

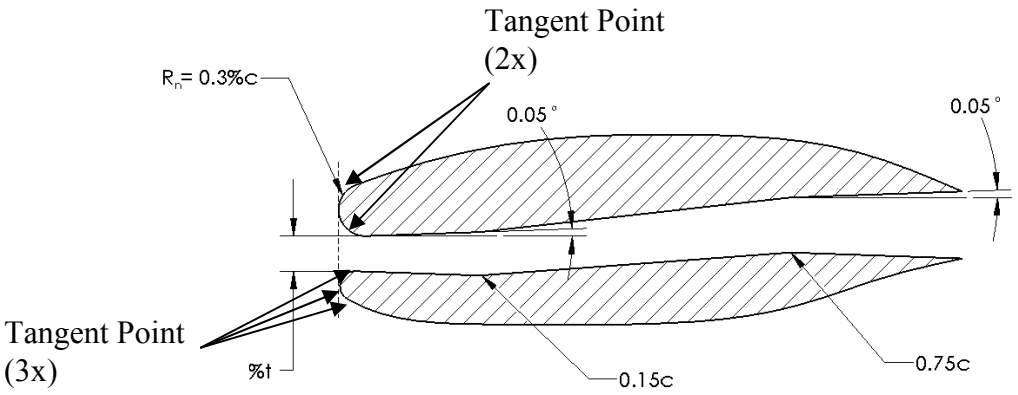

Figure 3. Channel Geometry of 8%, rounded LE (cr6c8), Not to Scale

For sharp leading edges the process was slightly modified. The center of the channel was not aligned with the baseline leading edge point because of the asymmetry of the airfoil. In order to make an inlet for the channel to be the correct size and the lips to be located at the same chord position, the height of the channel was calculated and then placed at the chord location where the height of the airfoil matched the height of the channel. The leading edge for the sharp lips was much closer to the original leading edge, located at .003057c for the 12% channel as opposed to 0.01609c for the rounded lip 12% channel. A sample of what the geometry of a sharp leading edge airfoil can be seen in Figure 4.

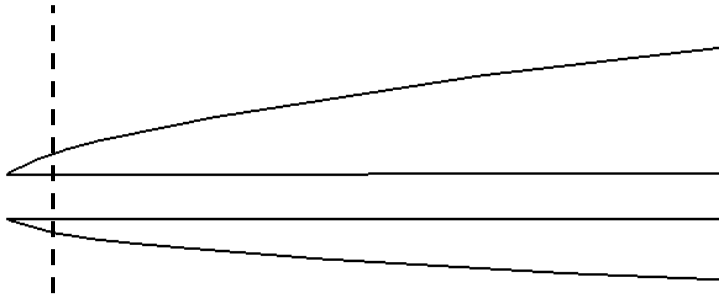

Figure 4. Sharp Leading Edge for 12% channel (cr0c12)

As the flow travels down the channel, the boundary layer grows. If subsonic flow is present in the channel, the airflow will speed up because the channel acts similarly to a converging nozzle. In order to minimize this effect and keep the flow from going sonic as much as possible, a small angle of 0.1° was put into the channel walls to make the channel expand slightly which corresponds to previous studies (Ruffin, 2000). Once this angle was established, the height of the exit portion of the channel could be set. The location of the exit was based on the principles established for the sharp leading edge channel, but applied at the trailing edge. The location where the thickness of the airfoil matched the height of the channel gave the position of the exit of the channel. Both trailing edge surfaces were sharp.

After both exit and inlet locations of the channel had been created, the inner geometry of the channel was determined. Multiple channel geometries were considered, but the basic channel used for most cases was a two kink channel. The two kink channel contained kinks in the channel at the 0.15c and 0.75c locations. The kinks were necessary because of the cusp that was present at the rear portion of the airfoil. The channel needed to be raised up above the inlet position to satisfy the trailing edge location requirements. The basic geometry was formed by creating a horizontal duct that started from the leading edge and extended to the 0.15c spar location. The half angle of 0.05° was also implemented. Overall this gave a larger duct radius but the same centerline position as the initial inlet to the channel. A similar technique was used for the trailing edge but in reverse towards the 0.75c spar location. After the channel positions were set at the spars, the two channels were simply connected to form a continuous flow path. A diagram of a

2 kink channel airfoil can be seen above in Figure 3 and in Figure 5. Airfoil models with an 8%, 10%, 12%, and 16.6% channel height were constructed.

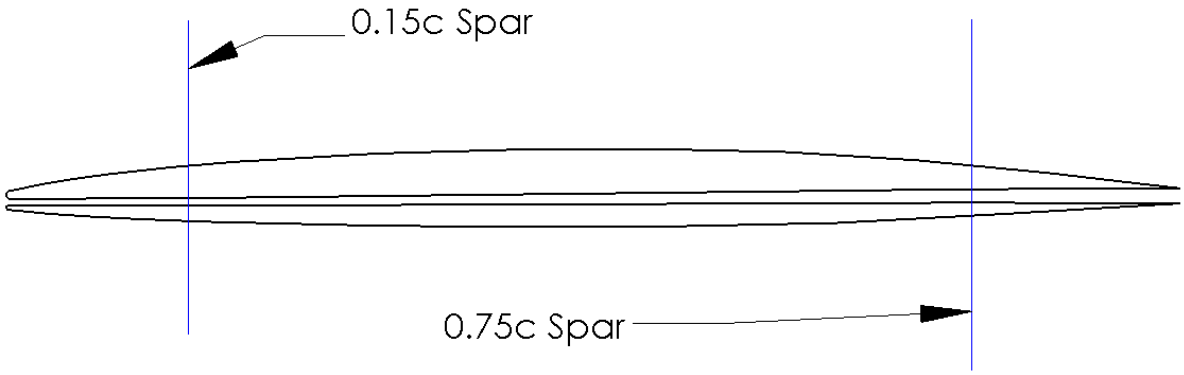

Figure 5. NACA 66-206 with channel geometry implemented

Two other channels were also examined, one with only one kink and the other that was a simple straight channel. As before, after both the inlet and exit locations and heights were set, the channel geometry was created. The straight channel geometry connected the inlet and exit of the channel with a straight duct. The channel height was not constant because of the growth factor in place to compensate for the boundary layer growth. The one kink channel geometry was set from the exit portion of the channel. From the exit, a horizontal channel was projected towards the 0.15c spar location. The boundary layer growth angle was included, causing the duct radius at 0.15c to be smaller than that of the exit. The final portion of the channel was created by connecting the inlet to the channel at 0.15c, causing only one interior kink to be present in the channel.

Baseline Airfoil Grid Generation

The basic grid used for meshing was an H-grid. The flow field outer boundaries were placed one chord length in front of the airfoil and 4 chord lengths from the trailing

edge of the airfoil. The wedge-type design can be seen in Figure 6. The shape was designed for Mach cones for a freestream speed of Mach 2.5 to extend from the airfoil and hit the outlet boundary. Other supersonic freestream speeds were also tested. For slower speeds the shock and expansion waves did interact with the upper and lower freestream boundaries. This interaction was downstream of the airfoil, and because of the supersonic nature of the flow, they did not affect the air around the airfoil itself.

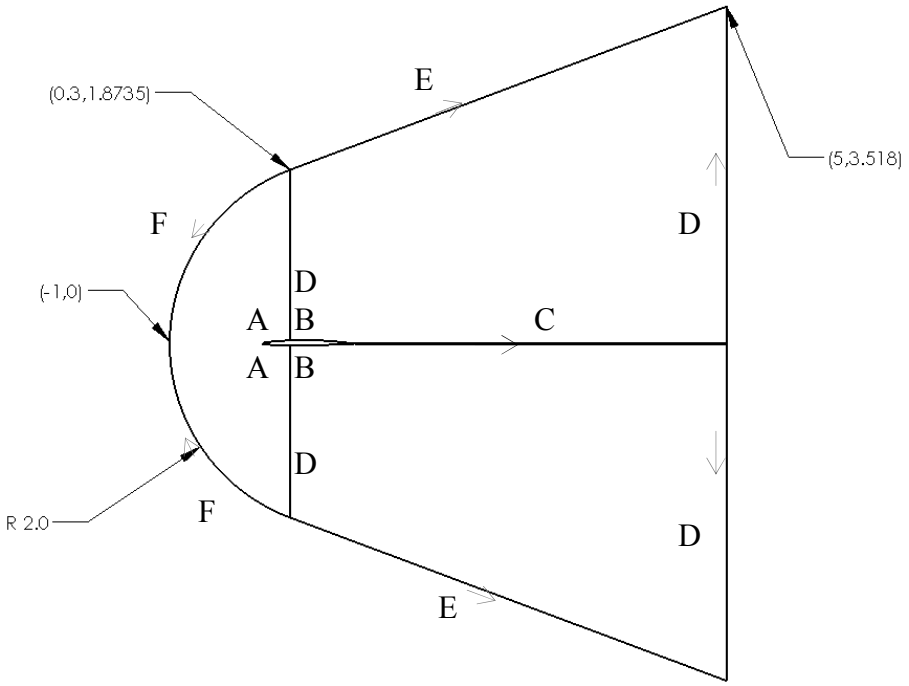

Figure 6. Initial Meshing Edges for Farfield Boundary Conditions and Airfoil

In order to construct the structured grid, the airfoil was split at 0.3c on both the upper and lower surfaces. This split the flow field into three main sections: front, upper back, and lower back. All edges were then seeded and meshed to create the structured mesh according to the Table 1. Refer to Figure 6 for locations.

Table 1. Seed Parameters for Initial Mesh

Edge	# of Elements	Clustering	Boundary Layer	Boundary Condition
A	50	First Length 0.02	No	Wall
B	50	First Length 0.02	Yes	Wall
C	60	First Length 0.01	Yes	Continuum
D	80	First Length 0.0014	No	Continuum/ Outlet
E	110	First Length 0.02	No	Farfield
F	50	First Length 0.025	No	Farfield

A boundary layer was put in on edges B and C in order to make the cells be as orthogonal as possible. The more orthogonal the cells, the easier and more accurate the computation can be (Tannehill, pg 679-713). This was especially important in the boundary layer so an accurate model of the flow in the boundary layer could be achieved. The height of the first cell was placed at 0.0014c. This caused the first cell node above the airfoil surface to have a y^+ value of less than 300. This placed it within the log layer so wall functions could be used (White, Fluent). This cell was adapted later to have a y^+ value of less than 100 so more accurate wall functions could be used to predict the boundary layer. The boundary layer was not implemented on the front of the airfoil because the leading edge, although rounded, skewed the mesh when a boundary layer grid was specifically implemented. Instead, the mesh was automatically sized in this area. The cells ended up being closer than 0.0014c so the boundary layer could still be accurately determined and the overall mesh quality was less skewed.

The interior mesh was then constructed using quad cells and a mapped structure. The total cell count was 25,600 for the baseline airfoil. An overall mesh can be seen in Figure 7. The boundary conditions for each edge can be seen in Table 1. The pressure farfield inlet boundary condition was at a 35,000 ft standard altitude, with the freestream flow at Mach 2.5. This gave a pressure of 23,842 N/m^2 and a temperature of 218.8 K.

This corresponds to a Reynolds number of 9.8 x 10^6. The pressure outlet condition on the outside boundary for the D edges was the same as the farfield. Walls were obstructions to the flow. The defaults were used for temperature and no heat flux was allowed into the walls. This would introduce a source of error into the analysis, but the amount of heat flux occurring was beyond the scope of this thesis.

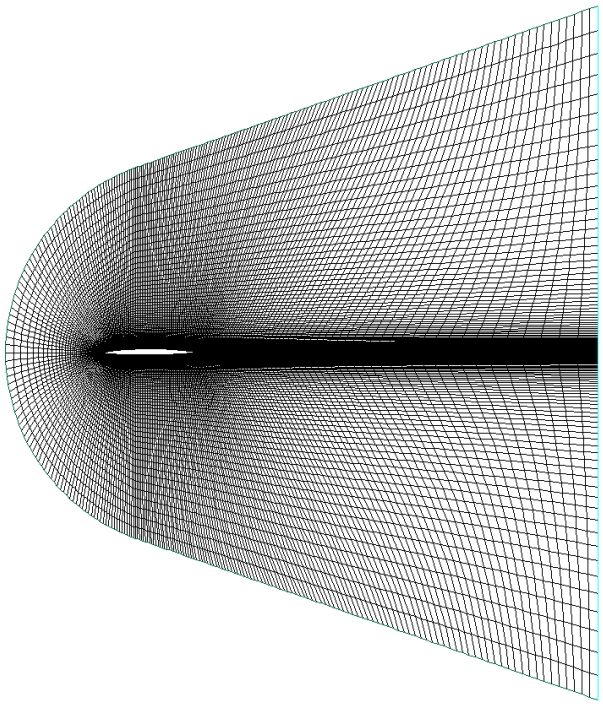

Figure 7. Structured Mesh profile for Baseline Airfoil

Channel Airfoil Grid Generation

The initial grid generation for the channel airfoil was the same as the baseline airfoil. However, there were some elements that needed to have special considerations. The baseline mesh was basically split into two halves with cells added before, in, and after the channel. The initial number of cells in a vertical slice of the channel was 6 cells. This was increased during the gradient adaptation process, however, to bring the y^+ value in the channel to less than 100. From the inlet to the exit, 100 elements were placed along

the chord length. These cells were clustered at both ends in order to match the exterior mesh. Typical values were 0.0014c for the first element and 0.008c for the final element length. This six cell count was extended from the exit of the channel all the way to the pressure outlet boundary. In the front of the channel, the two lips leading into the channel were split at their leading edge points. On the exterior portion of the leading edges, the normal 50 element and clustering was performed. Directly in front of the channel, a small area was created that was not a structured mesh. Instead a quad paver mesh was required as seen in Figure 8. This zone extended 0.0126c or nine boundary layer cells in front of the leading edge to match with the boundary layer from the exterior of the airfoil. The inner lips contained approximately six to eight cells for initial grid generation. All spacing on the inner lips was done to try and make the mesh match as much as possible the spacing from the exterior cells while keeping the inner cells orthogonal. In front of this unstructured zone, the structured mesh was resumed up to the farfield pressure boundary. Overall the total amount of cells in a typical channel airfoil mesh was around 27,000.

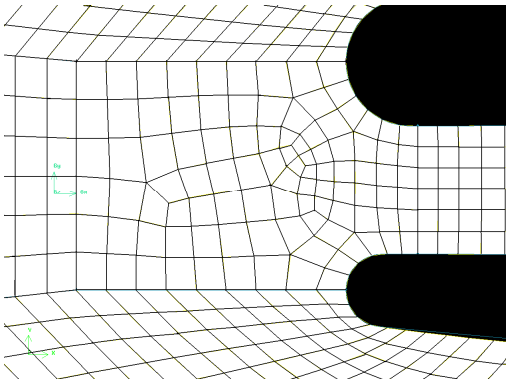

Figure 8. Unstructured Mesh at Leading Edge of cr6c10

CFD Analysis

All CFD cases were performed using the Fluent 2D double precision solver. Default criteria were used for most parameters. However, the convergence criteria for the residuals were set at 1e-6. At the default of 1e-3, only one or two gird adaptations would be performed and the bow shock formed would not be resolved correctly. If the residual tolerance was not achieved then the case was stopped after the lift and drag coefficients had reached steady values to at least 4 significant digits. The Courant number used for the cases was one.

An algorithm, or journal file, was created in order to consistently solve each mesh introduced. Initially, all meshes were solved for the condition of Mach 2.5, 35,000 ft altitude, 0 angle of attack freestream flow. First, the flow field was initialized to a uniform flow. The initialized flow had a similar pressure and temperature field as that of the inlet pressure farfield condition. However, it was found that if the flow was initialized to about Mach 2.0, the flow could resolve before being subject to the Mach 2.5 flow which would solve down from the boundary conditions. This allowed the Courant number to be one. Initial runs required the Courant number to be much lower, around 0.2, in order to have the solver not diverge initially which increased the solver time.

The first iterations of the solver used laminar flow conditions. Even though the flow can be considered fully turbulent, since the Reynolds number is 9.8×10^6, the laminar flow solver was quicker than the turbulent equations. The flow was solved for 10,000 iterations, or unless the residuals convergence criterion were met. Usually the flow converged or became steady state around 4000 iterations. This allowed the flow to

become resolved and avoid divergence errors that surfaced when the initial iterations were using the turbulent equations only.

In the second set of iterations, the k-epsilon turbulent model was run. This first run turbulent solver was able to solve for the basics of the fully turbulent flow field. By running it for 10,000 iterations, the flow was sufficiently resolved to use the k-omega turbulent solver. If just the k-omega solver was turned on directly after the laminar flow solution had converged, a maximum turbulent viscosity error would appear. This meant that the laminar to turbulent ratios were too large because of the skewness of the cells. However, after solving the turbulent equations initially using the k-epsilon model, the error would still appear for the k-omega solution but would resolve itself quickly within about 100 iterations instead of diverging. Standard wall functions were used while solving for the k-epsilon 2-equation model.

The next step was to solve for the k-omega turbulent model using the shear stress transport model. The initial run was for 2,500 iterations. This allowed the flow to begin to be resolved by the k-omega 2 equation model. For some flows, especially those with a sharp leading edge, this was enough to initially converge the flow field. It also allowed the turbulent viscosity error to be resolved. After these preliminary iterations, 2,500 more iterations were performed. However, at this point gradient adaptation was used to refine the grid around flow features.

Pressure gradient adaptation was used first for the 2,500 iterations. The pressure adaptation helped to resolve the flow around the shocks and expansions present in the flow field because these are areas where a large change in the pressure was present. If not, the solution often oscillated back and forth around cells where these high gradient

areas were. This was especially true for the bow shock regions which would move the bow shock back and forth between coarse nodes. The grid was adapted every 100 iterations. Refinement used an aggressive scaling scheme with all cells above a scaled number of 0.9 being refined. Initial refinements averaged about a quarter of the cells in the flow field. The cells were allowed to be refined up to two levels. This meant that one cell could be split into four cells twice for a total of 16 cells. Besides refinement, the cells were also coarsened. The grid was not allowed to be any coarser than the initial grid made in the meshing program. However, if cells had been refined, they were subject to a scaled coarsening criterion of less than 0.3. If all four cells that were originally refined were now below this 0.3 limit, the cells would coarsen back to the original cell. This allowed the bow shock to traverse the area in front of the airfoil as it resolved with the refined zone traversing with it, coarsening as the bow shock resolved to a new location. The mesh was checked every 100 iterations for both the refining and coarsening criteria.

After the first two level adaptations had occurred for 2,500 iterations, a third level of adaptation was allowed. The sequence was broken up because of the large number of cells used with three levels of pressure adaptation caused longer computational times. This gradient adaptation was in place for 10,000 iterations. When this had completed, the final adaptation sequence was run. The airfoil boundary cells were adapted to have a y^+ value of less than 100. This adaptation only took 2 or 3 checks to get all the cells to be below 100, but a check continued to occur every 100 iterations for the entire 10,000 iterations. The value of 100 was chosen because it allows a higher fidelity boundary layer model such as Sutherland's model to be used, but was above 30 where the buffer layer is located so the approximations are still valid. No coarsening was implemented. In initial

runs, the grid adaptation would place the first node at a y^+ value of 50-100, at which point no further refinement was allowed. It was verified that no cells were less than 30 once the run was finished. After 10,000 iterations every single case run was either at steady state or the residual tolerances had been met already. The solution sequence is summarized in Table 2.

Table 2. Baseline Flowfield Solver Sequence

Flowfield solver	Grid adaptation	# of iterations
Laminar		10,000
k-ε turbulent		10,000
k-ω turbulent		2,500
k-ω turbulent	Pressure (2x level)	2,500
k-ω turbulent	Pressure (3x level)	10,000
k-ω turbulent	y+ (<100)	10,000

Once the initial Mach 2.5 case had been solved for, other data points were desired, especially at angle of attack. An α value of 6° was used to ensure that positive lift coefficients for the airfoil would be measured. To obtain these new data points, a new algorithm was introduced to solve the flow field. Since the flow had already been solved for a k-omega model, the turbulence model used was not changed. Once the boundary conditions had been set to their new value such as at an angle of attack or a different speed, the mesh was once again subject to pressure gradient adaptation. The same model was used as before. The refine/coarsen scale levels were again at 0.9/0.3 and the maximum level of refinement was still set at 3 levels. This often coarsened up the cells in the boundary layer, causing the y^+ value to increase. To rectify this, after 20,000 iterations of pressure adaptation, the adaptation process was once again switched to the y^+ adaptation. For 10,000 iterations, the model was again only refined to get the boundary layer cells to be under 100. Once again, after these 30,000 iterations, the case was at

steady state or the residual tolerances had been met. Along with the first run at Mach 2.5, cases were examined at Mach 1.5, 2.0, and 3.0.

Structural Analysis

The first step to any structural analysis is to determine the loads that the structure will be experiencing. PanAir, a panel code, was used to approximate the loading the wing would incur during Mach 2.5 flight (PanAir). The implementation of the channel design was to be on a realistic wing design. Two reference aircraft were combined to make a typical design model for a supersonic transport (Rinoie, Wright). The resultant reference wing planform can be seen in Figure 9. A flat plate model of the planform was then constructed in PanAir and the resultant lift distribution was determined. Given a 665,000 lb base cruise weight for the aircraft (Wright), the forces on the wing were determined.

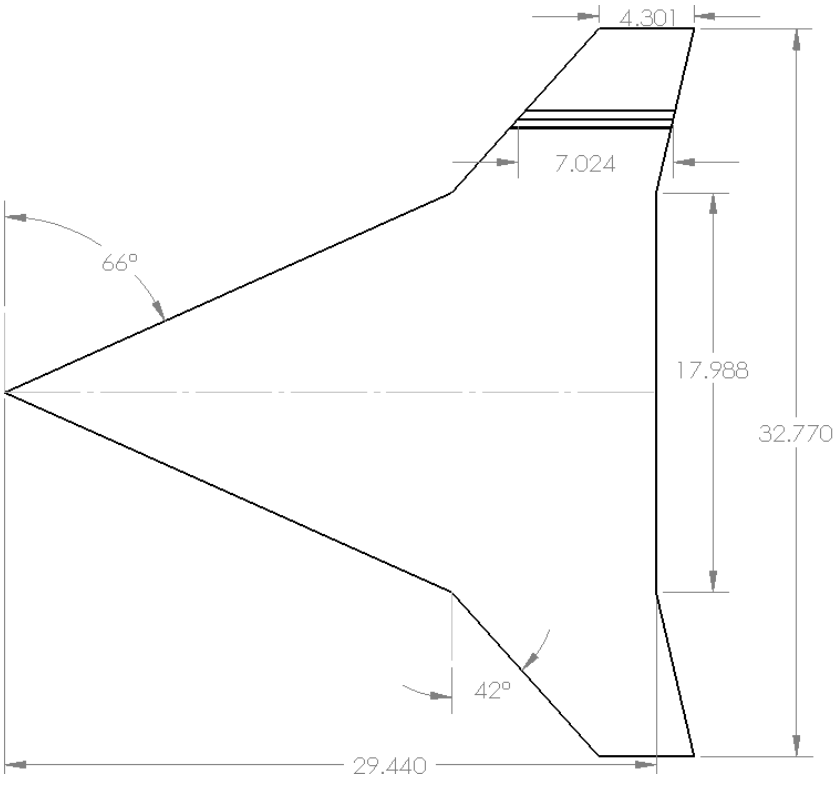

Figure 9. Baseline Wing Planform for Supersonic Transport (m)

The midpoint of the outer section of the cranked arrow wing planform was chosen as the representative section of the wing to be the basis for the structural analysis. This section was chosen because it would be far enough away from the engines and loading in this section is not as large as the inboard section. Also, if the performance was enhanced in a particular section of the outboard portion of the wing, it could be applied to other outboard portions other than the representative section. The section was between two ribs, spaced at a typical width of 30in, or 0.764 meters. The chord length was 6.765m for a rib at the midpoint location, with the chord length of 7.024m for 0.382m location inboard of the rib, where the mid channel would be located.

The 7.024 chord position became the center of the design of the spar. For simplification purposes, the spar height was not tapered as it would be between ribs. Instead the spar height was held constant at the height at the baseline chord position. For the 0.75c spar, this height was about 0.274m as opposed to the 0.15c spar which was 0.298m. The forces present at the end of the spar, where the rib would attach, were a moment of 13,524 Nm and a vertical force of 2,075 N determined from the air loads. The interior pressure loads were determined from the 2D airfoil results. These were resolved into point loads that could be applied at the spar locations.

The material selected was a basic aluminum. AL 2024-T4 is a typical aircraft aluminum with good fatigue properties (Matweb). A summary of its material data can be seen in Table 3 (Beer, pg.747).

Table 3. Mechanical Properties of Aluminum 2024-T4

Aluminum	density (kg/m^3)	Ulimate Tension (Mpa)	Ultimate Shear (Mpa)	Yield Tension (Mpa)	Modulus of Elasticity (Gpa)	Coefficient of Thermal Expansion	Ductility (% elongation in 50mm)
T4	2800	480	280	325	73	23.2	19

An I-beam design was used to determine the size of the spar. The lower limit for the web thickness was set at 2 mm and the flange thickness limit was set to 3 mm for this simple structural model. Using a gradient based optimizer in Matlab, the cross section that had the least amount of area that would not fail in tension with the given loading was determined. The moment arm of the force was considered to be the distance between two ribs, 0.764m, optimizing the cross section of the spar at the next rib location, at the opposite end of the spar where the rib loading was assumed to be. The cross sections for both the 0.15c and 0.75c spar are seen in Figure 10. The next step was to take the optimized cross section into the finite element program ABAQUS. The cross section was then extruded a distance of 0.764m to form the basic I-beam structure. This was not an optimized beam structure for the entire beam for the given loading conditions, but the cross section at opposite end of the loading condition was optimized for tensile stress.

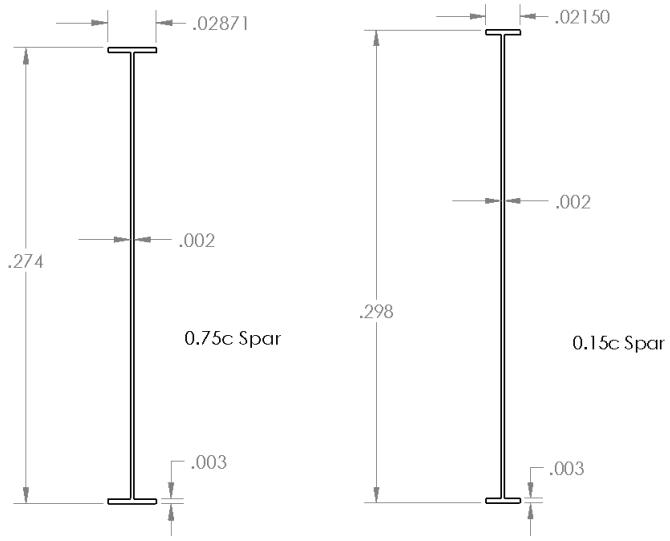

Figure 10. I-Beam Profiles for a) 0.75c spar and b) 0.15c spar (m)

In the I-beam, various channels were cut out in order to examine the effect of placing a channel through the wing. The mid point location of each cutout was located

centrally in the spar at 0.382m from either end. The vertical location on the spar was determined by the location from the 2D airfoil models. Also the size of the hole was determined from the airfoil model which was different since boundary layer growth was taken into account.

The first cutout examined was a circular channel. Material was removed from the I-beam and discarded. Models were built for the 8%, 10%, 12%, and 16.6% channel. Other circular channels were constructed by not discarding any material. The original hole was still cut out, but the material was then applied around the hole to reinforce the cut out. The material was added concentrically around the original channel cutout increasing the thickness by 1 mm on each side, effectively doubling the thickness of the web at the edge of the hole. This did not add any new material.

Other channels were considered for the 12% t/c channel. The next basic channel considered was a square channel. The width of the square channel was the same size as the diameter of the 12% circle cut out. This was also tested using a reinforced channel as well. The next channel examine was a slot. This consisted of a rectangular cutout section the same height as the original circular channel but with varying widths. At either end of the rectangular cutout, a half circle cut was also implemented. This made a continuous edge instead of the four sharp discontinuities encountered with the square cut. The widths of the rectangular portion of the slot examined were the same size as the square, 25% of the spar, 50% of the spar, and 75% of the spar length. The slot geometry and sizing for the configurations can be seen in Figure 11.

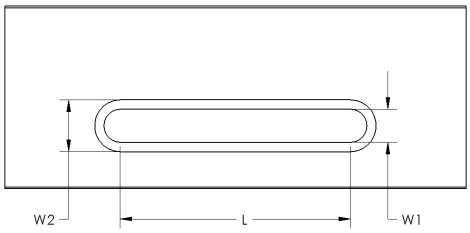

Type	Size 0.15c Spar	Width L (m)	Cutout w1 (m)	Reinforced w2 (m)
circle	12%	-	0.0538	0.0760
circle	8%	-	0.0370	0.0524
circle	10%	-	0.0454	0.0642
circle	16.6%	-	0.0734	0.1036
slot	12%	0.053	0.0538	0.0745
25% slot	12%	0.191	0.0538	0.0800
50% slot	12%	0.382	0.0538	0.0845
75% slot	12%	0.573	0.0538	0.0874

Figure 11. Slot Geometry and Sizing (12% Height, 50% Slot Shown)

For the 50% slot, multiple geometries were examined to determine trends after initial analysis had been performed. In order to optimize the beam more, the flange closest to the slot, the bottom flange, was tapered to different amounts to try and minimize the effect of the slot on tensile failure. The top flange had a constant cross section. In all tapered cases, material was eliminated from the loaded side of the spar and added to the opposite part of the spar where the higher stresses were. This did not change the amount of material being added, which meant the weight was the same. A 10% high slot was also constructed, as well as an 11.4% high slot for the 50% width slot geometry. These slots were also examined for reinforced holes as well.

After each cutout geometry had been created, the geometry was meshed and examined before a new geometry was formed. For meshing purposes, solid elements were used for all parts of the I-beam. For the basic cross section, the seeded elements can be seen in Figure 12. For edges F, along the spar, the spacing was at 0.01m. For all edges

the spacing was uniform and not clustered. The recommended number of elements in a thickness was desired to be at least four, which set the number of elements for edges B (ABAQUS). This was because solid elements do not have the ability to directly carry bending boundary conditions so four elements allows enough bending to occur between the elements. The web was only two elements thick, but in the critical bending direction it was 20 elements thick.

Edge	# of Elements
A	16
B	4
C	7
D	20
E	2

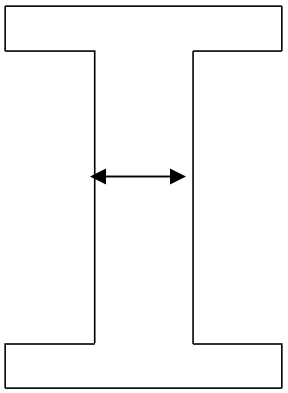

Figure 12. Seed Mesh Parameters for I-Beam Profile (Not to Scale)

Once the I-beam mesh was set, boundary conditions were applied to the spar. At the rib location without loading, a simple pin joint constraint (123) was implemented as the boundary condition. As mentioned above, the solid elements cannot directly carry rotation, so in essence all six degrees of freedom were constrained. The loaded end would also be attached to a rib, but be free to rotate. In order to simulate the attachment, all end elements were made to move together. This was achieved by embedding beam elements into the end shaped in the cross section of the solid elements. These beam elements were orders of magnitude more rigid than solid elements with a tensile stress limit of 10^{15}

N/m^2. This made the elements very rigid so they would not deform under the loading conditions and hold the cross section shape at the loaded end of the beam.

The 2,075 N force load was applied on the top of the beam at the midpoint of the flange as a concentrated load. In order to not have a stress concentration where the moment was applied, the moment was applied using a force couple system on the edge of the beam. The top half of the end cross section had a uniform compressive pressure force applied to it whereas the bottom had an equal and opposite pressure force, providing the required moment. When the flange size changed for the bottom flange, the pressure force acting on the flange face was modified to provide the same resultant force as before. Figure 13 shows the boundary conditions.

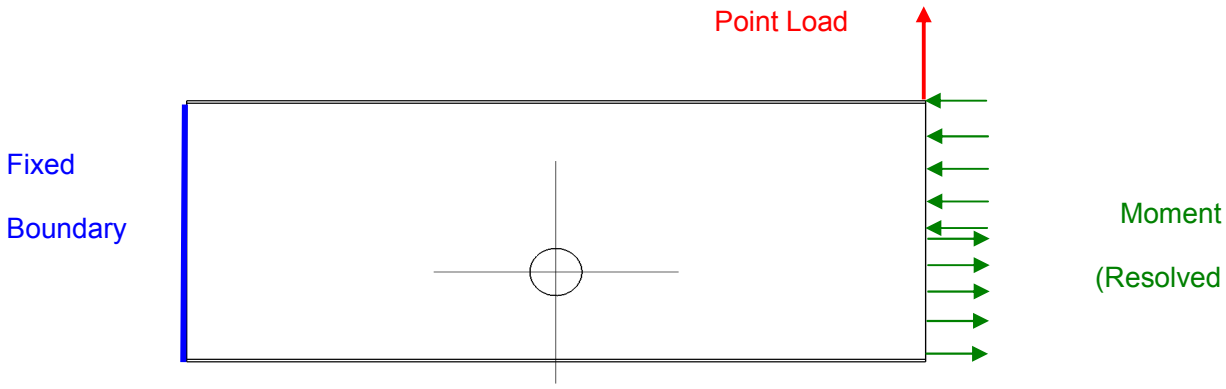

Figure 13. Free Body Diagram of Baseline Loading Conditions

The main web had a different mesh for each different channel geometry. ABAQUS was allowed to use a quad paver mesh after the edges had been seeded. For the circular channel, 40 nodes were placed on the inner face of the cut. This gave smaller cells near the cut out which was needed to more accurately capture the stress concentrations. When the reinforced hole geometry was implemented, another solid element layer was created that matched the layer underneath in the main web. The mesh

around the hole was now four elements thick instead of two with an unreinforced hole. For the circle and slot geometries, the ABAQUS automatic meshing protocol gave meshes with even spaced, regular cells that were denser near the slot. For the square section, originally ABAQUS gave meshes that were very irregular with large cells mixed in with small cells. If a finite element run had been performed on this mesh, the large gradients present would have most probably skewed the data. To avoid this, the main web was partition into two regions: the main web, and a circular area which the square hole was contained within. This allowed the cells in the main web to act as if a circular hole was present, and the mesh around the square hole was much more regularly spaced. The final square mesh can be seen in Figure 14, which was similar to the other meshes for circle and slot channel cutouts.

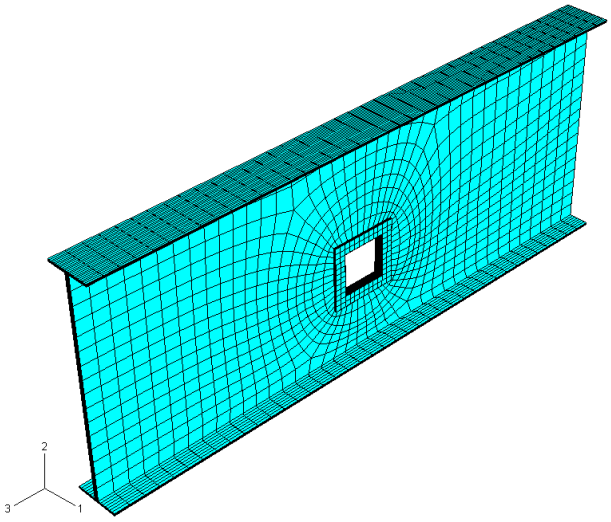

Figure 14. Final Mesh for Reinforced Square Cutout, 12% Channel

3D Wing Analysis

The three dimensional wing analysis using CFD techniques had a similar process to that of the 2D airfoil. First the geometry was constructed using Solidworks. The

models were then imported into the meshing program Gambit and finally the flow field was solved using Fluent.

Baseline Model Generation

The baseline solid model was based off of the original NACA 66-206 airfoil. The model was scaled up to a chord length of 7.024 m, the chord length used in the structural analysis. The airfoil profile was then extruded a distance of 0.764 m, the size of the spar. This gave a 3D solid model of the wing between two ribs based on the reference airplane. However, this was not the same as the reference aircraft because wing sweep was not added in. In order to match with previous analyses, the wing model was then scaled down to a chord length of one. This allowed Reynolds number matching to occur while providing a model that would still be the same basic rib to rib unit as the larger reference aircraft.

11.4% Channel Model Generation

The channel 3D model generated had the same outer structure as the baseline model. However, only a half model was used to take advantage of the symmetry planes present at the rib location and also at the center of the channel. Thus a more detailed mesh could be created later on.

The slot geometry chosen for the 3D model was determined by combining the structural analysis and the 2D airfoil analysis results. From this, an optimal slot of 11.4% t/c height and a 50% width slot was found. The slot was extruded onto the half model as a cut. The 2D 11.4% model geometry was projected onto the symmetry plane and a straight cut to the 50% width mark was made. The curved portion of the slot was also extruded

into the half model. Some modifications had to be made to allow the geometry to be created. For the leading edge, the circular part of the slot made a blind cut straight out the front of the leading edge. This provided a straight path for the air flow to enter the channel for both the rectangular and circular portions of the slot. The leading edge of the 3D case was a sharp leading edge. For the trailing edge, the rectangular portion of the slot had an unobstructed exit path. A simple straight cut for the circular portion did not allow the flow to exit freely. At the trailing edge, the airfoil has a slight droop to form the cusp needed promote lift. When a straight cut was made through this section, the wing model curved back into the flow. To allow the flow to carry straight out the back, a draft angle of 3° was implemented. This effectively expanded the circular cut by three degrees into a cone type cut. From this, the flow was allowed to accelerate smoothly out the exit. The cut was still not ideal because of a lip present on the lower part of the cut that could not be eliminated entirely because of the limitations of the CAD modeling program. Figure 15 shows the final solid model geometry from different angles.

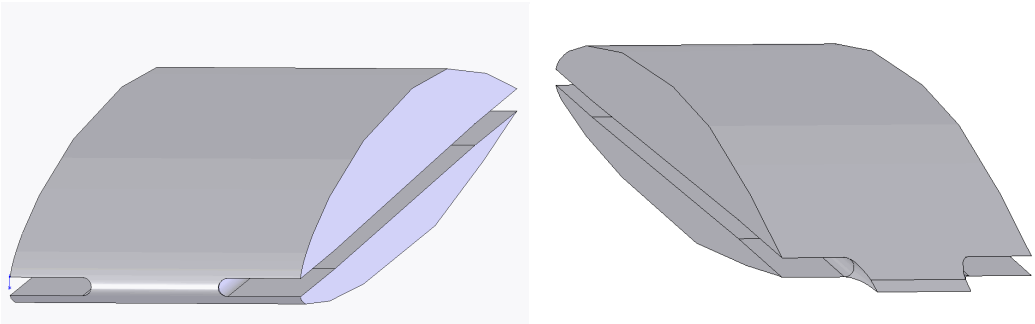

Figure 15. Slotted Solid Model for 11.4% channel a) Leading Edge and b) trailing edge

Baseline Wing Initial Grid Generation

The grid generation for the 3D wing was the same as for the baseline airfoil. Two symmetry planes were created at each rib location. The grids used for the baseline airfoil were again constructed on the symmetry planes. 12 nodes were seeded on the edges that connected both symmetry planes. A structured mesh was created using hexahedral cells. The total cell count was about 300,000 cells.

11.4% Channel Initial Grid Generation

For the channel 3D model, a half model of the baseline model was used to take advantage of symmetry as described above and allowed a more detailed mesh for the same amount of computational cells. For the rib symmetry plane, a 2D cut was exactly the same as the 2D baseline airfoil. The major components of the symmetry plane were meshed exactly the same as in the 2D case. The only difference was at the very leading edge. The leading edge was split at the location where the 11.4% channel would have intersected it. A total of 10 cells were placed at the leading edge. These 10 cells were subtracted from the other surface edges to maintain the total number of cells around the airfoil at 200. The airfoil was also split at the trailing edge in the same way. The wing mesh at the leading edge can be seen in Figure 16. The leading edge near the slot can appear to be concave towards the inner part of the wing. Geometrically, the circular closeout follows the airfoil section shape, and because of this, the cells are more skewed around this surface which can give the illusion in a two dimensional view.

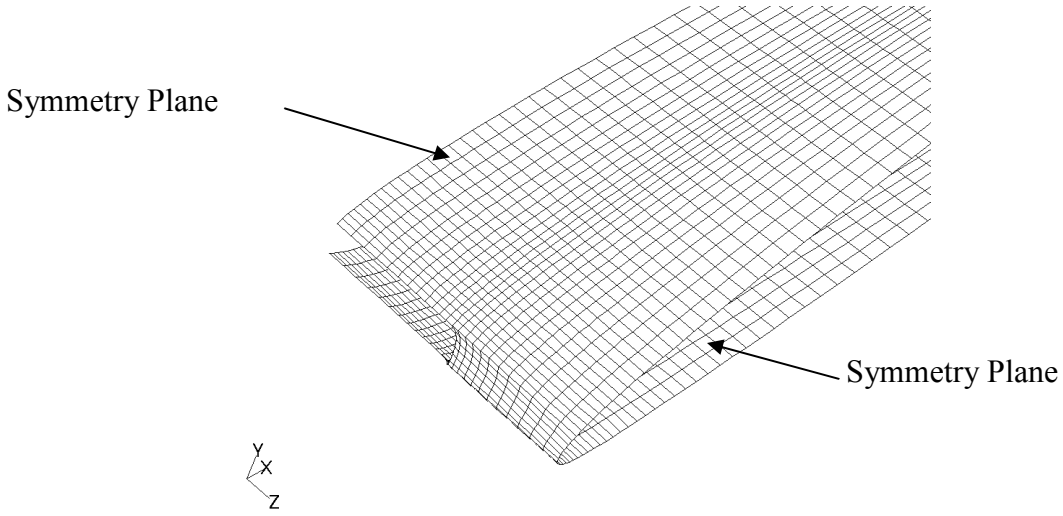

Figure 16. Leading Edge Surface Mesh of 11.4% Slotted Wing

For the channel symmetry plane, the leading and trailing edges were continuous. In order to form a structured mesh, the baseline airfoil was projected onto the symmetry plane. The entire outer portion of the airfoil was meshed the same as the rib symmetry plane, allowing a mapped mesh to be created. In front of the slot, the leading edge face had cells created on both sides which treated the face as part of the continuum whereas on the solid part of the airfoil the cells were only on one side and the face was considered as a wall boundary. Even though the mesh was the same for both sides, the flow characteristics were much different for each plane. The mesh created was 24 cells across which were clustered towards the middle of the airfoil to capture the interaction of the slot and no slot regions

Inside the slot itself, three regions were created. The first was the heart of the channel which was meshed with the same criteria as the channel in the 2D airfoil. The regular shape of this region can be seen in Figure 17. A mapped hexahedral mesh was created. For the leading and trailing edges, hexahedral cells were again used, but a Cooper scheme was adapted in order to allow a structured mesh to work. The faces that

seeded the Cooper scheme of the leading edge can be seen in the figure. These are the circular sections at the front of the channel. The total number of cells used was about 670,000.

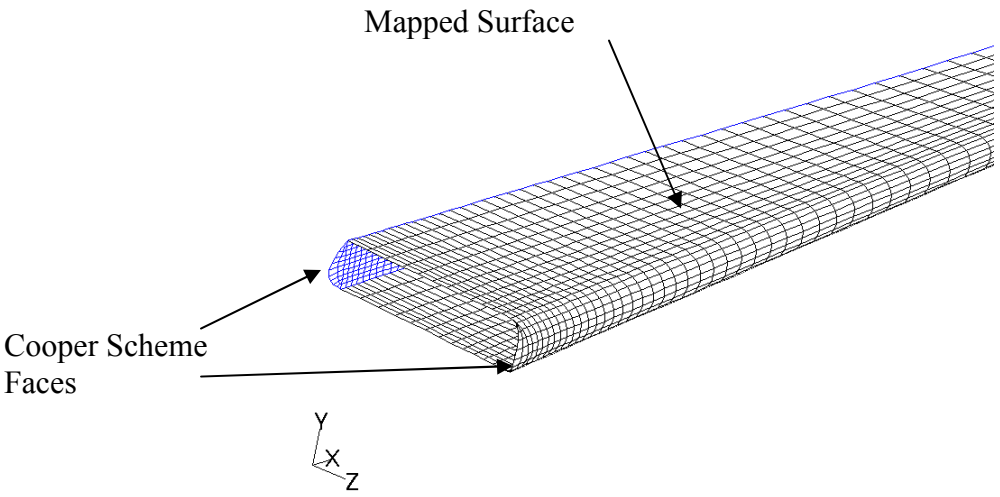

Figure 17. Interior of 11.4% Slot, Surface Mesh

Boundary conditions for the 3D wing models were the same as in the 2D airfoil analysis. The pressure farfield boundary was still set to Mach 2.5, 35,000 ft standard altitude however the flow was placed at an angle of attack of 6°.

CFD Analysis

All 3D CFD cases were performed using the Fluent 3D double precision solver. Default criteria were used for most parameters. The convergence criteria for the residuals were again set at 1e-6. The residual tolerances were never achieved but were set to allow the solver to continue to iterate. The case was stopped after the lift and drag coefficients had reached steady values to at least 4 significant digits. The Courant number used for the cases was one.

For faster convergence, multi-grids were used. The multi-grid scheme allows for faster convergence times by detecting low frequency errors that occur in finer grids (Tannehill, pg.165). Four multi-grid levels were used to speed up convergence with two residual updates.

To solve the flow field, a set algorithm was not used. Since only two cases were being performed, specific techniques to approach the problems encountered were used. These were based on knowledge gained from the 2D analyses. For both cases though, the same general approach was used.

With the multi-grid technique in place, the flow field was initialized as in the 2D airfoil analysis. The first run was 1000 iterations for the laminar flow. After 1,000 iterations, the lift coefficient was steady and the drag coefficient was not changing to three significant digits. Because of the multi-gridding scheme, less iterations could be used to obtain the same amount of accuracy as a plain solver. Next the k-epsilon turbulent solver was turned on for 2,000 iterations. Standard wall functions were again turned on.

The 2 equation k-omega turbulent was the third solver type used. For both the channel and baseline wings, the turbulent viscosity ratio limit was present in a few cells at the start of the k-omega iterations. However, after about 2,500 iterations, the solver was able to eliminate the maximum turbulent viscosity error. The solver was allowed to continue to run until about 6,000 iterations had been completed. Then adaptation over the pressure gradient was turned on.

Only two levels of pressure adaptation were used for the three dimensional model because of the large amounts of cells involved. The refinement minimum limit was changed to a more less aggressive scheme of 1.4 from 0.9 in order to limit the number of

cells. Also, unlike the two dimensional solution, the pressure was adapted every 200 iterations. This was done because the multi-grid levels were the most expensive part of the computation and had to be recreated after every adaptation. Once stability to four significant digits had been obtained, about 5000 iterations, the y^+ gradient was turned on for 1500 iterations as in the two dimensional analysis. Fewer iterations were needed to adapt the grid for y^+ as opposed to pressure. After four adaptation checks, the first nodes all had a y^+ of less than 100 and no further refinement would be allowed. It was verified that the lowest cell was greater than 30 in order to allow for the use of wall functions, similar to the 2-D cases. Once verified, gradient adaptation was then turned off to allow the computation to proceed without the expensive recomputation of the multi grids. After 2500 more iterations and convergence to four significant digits, the final results were tabulated. The slotted 3D wing section grew to a cell count of more than 1.7 million cells. The solution sequence is summarized in Table 4.

Table 4. 3D Flowfield Solver Sequence

Flowfield solver	Grid adaptation	# of iterations
Laminar		1,000
k-ε turbulent		2,000
k-ω turbulent		6,000
k-ω turbulent	Pressure (2x level)	5,000
k-ω turbulent	y+ (<100)	1,500
k-ω turbulent		2,500

CHAPTER 3

Experimental Results

Three different analyses were performed. The first analysis performed was an aerodynamic analysis on a 2D section of the airfoil. Next a 3D structural model was analyzed which explored the effects of the supersonic channel airfoil in a plane orthogonal to that of the 2D airfoil. The structural model characteristics combined with the aerodynamic model to create a three dimensional aerodynamic model.

2D Airfoil Analysis Results

In order to fully capture the flow field accurately, the grid was adapted two ways. Initially the grid was adapted in areas of high pressure gradient. This captured the major flow field characteristics such as leading edge shocks, expansion waves, and oblique shocks. Figure 18 shows how the grid adaptation algorithm was able to adjust itself to the areas of high pressure gradient. It also gave an overall rough view of what the converged flow field looks like. The bow shock was clearly visible at the front of the airfoil as were the oblique shocks located at the trailing edge. Pressure gradient adaptation was not the only area of refinement. The boundary layer cells were also refined to a maximum y^+ value of 100 in order to capture the boundary layer effects. Usually two refinements of the cells closest to the airfoil were required to reach the 100 limit threshold, but if necessary 3 refinements were allowed. At the end of each run, the y^+ values were checked and each time the cell values were below 100.

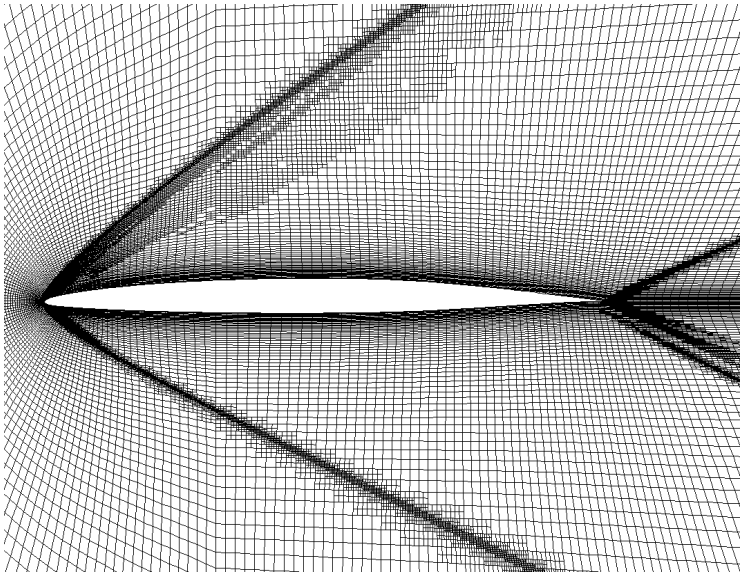

Figure 18. Adapted Grid for NACA66-206 at Freestream $M_\infty = 2.5$

Limiting the amount of grid adaptation to only two levels was also explored. The results can be seen in Table 5. The largest difference was for the pressure drag force which had a relative change of 1.3%. L/D, the parameter most looked at in this study, only differed by less than 0.1%. This gave high confidence in the overall data.

Table 5. Force Data for Diverging 8-16.6% Channel for Varying Refinement Limits (Newtons)

	Drag Force			Lift Force			
Refinement	Pressure	Viscous	Total	Pressure	Viscous	Total	L/D
2	2937	690	3628	16103	-66	16037	4.421
3	2974	684	3631	16107	-65	16041	4.418

In order to validate the progressive solver approach, comparison to experimental data can be used to check the model. For this study, the NACA 66-206 was examined at supersonic flight. No data could be found on the NACA airfoil at these speeds. However, Abbot has extensive subsonic data. The journal file that stepped through the progressive solvers from laminar to turbulent for all supersonic cases was also run at a speed of Mach

0.2. The lift coefficient was 0.159 (See Appendix A) which matches the 0.15 from Abbot. For a standard roughness airfoil, the drag is .0085 where the model gives .0075. However, since there is no matching case of experimental data at supersonic speeds, the validity of the model to absolute values can only be inferred. The confidence is high, though, in the trends in the data. This research was focused on seeing if a change in overall L/D could be achieved and a comparison to the absolute value is not imperative. This does leave room for future work to validate the CFD solver via experimental result.

The basic hypothesis was that by implementing the channel into the airfoil design, greater performance could be achieved. The first test run was a 12% channel airfoil compared to the baseline. The summary data for the fully turbulent flow is presented in Table 6. The performance was improved in some areas but hindered in others. As expected, the pressure drag force was decreased because the large stagnation region caused by the bow shock was dissipated into two smaller stagnation points on either side of the channel. The decrease was about 19.7% for the channeled airfoil. The viscous force was almost doubled. For a no-channel airfoil, the viscous drag accounted for 12.4% of the total drag. For rounded channel airfoil, the viscous drag accounted for 25.4% of the total drag. Even though the air going through the channel was subsonic, it still interacts with the side walls of the channel. Because of the doubling of the wetted area of the airfoil, the viscous increases from 325 N by 92.2% to 625 N. Despite the decrease in overall drag over the airfoil, the chord length of the channel airfoil was measured only 0.91c compared to the baseline airfoil. This altered the non-dimensional parameters used to calculate the coefficients. If both airfoils had the same chord length, the channel airfoil

would have a lower total drag coefficient than the baseline airfoil, 236 counts to 251. Instead, the coefficient was actually 259 counts of drag for the channel airfoil.

Table 6. Comparison of Channel and No-Channel Airfoil at M_∞= 2.5, 35,000 ft altitude, and $\alpha = 0$

	Drag						Lift						
	Force			Coefficient			Force			Coefficient			
CaseName	Pressure	Viscous	Total	Pressure	Viscous	Total	Pressure	Viscous	Total	Pressure	Viscous	Total	L/D
cr6c12m25a0	1836	625	2460	0.0194	0.0066	0.0259	-1546	5	-1541	-0.0135	0.00004	-0.0135	-0.63
c__m25a0	2287	325	2612	0.0219	0.0031	0.0251	-1227	3	-1223	-0.0118	0.00003	-0.0117	-0.47

For the lift forces at zero angle of attack and a freestream Mach number of 2.5, the NACA 66-206 gave a negative lift force. When examining the lift coefficients, adjusted for the chord length of each airfoil, it was found that the lift coefficients were around 0.01, very close to zero. This agrees with thin airfoil theory, which for a flat plate, lift is only created by the angle of attack at supersonic speeds (Anderson). Since the airfoil was not symmetric, the negative lift force could have been caused by the shaping of the airfoil which gives a slightly different angle of the flow along the edge of the airfoil.

In either case of lift or drag, the discrepancy in the chord lengths meant that the coefficients were based on different numbers. In order to non-dimensionalize by the same way each time, L/D was examined. This would eliminate the chord length from the non-dimensional calculation. However, at zero angle of attack the lift values were negative. This caused confusion about what value of L/D was actually better performing: least negative or greatest overall magnitude. In order to judge the performance of the airfoil, the ensuing runs were all placed at an angle of attack of six degrees.

The lift-to-drag ratio was examined at the freestream conditions of Mach 2.5, 35,000 ft standard altitude at an α of 6°. Three basic models were examined, the baseline NACA 66-206 airfoil, various rounded leading edge channel airfoils, and sharp leading

edge channel airfoils. At Mach 2.5, the baseline airfoil had an L/D of 4.12. Each rounded leading edge airfoil had L/D ratios that were less ranging from 3.87 for the 8% t/c channel to 4.06 for the 16.6%. As the channel got larger, more of the air flow that would have normally been a part of the stagnation region was diverted down the channel. This caused the severity of the stagnation point to lessen for each lip as the channel widened. In order to improve L/D to greater than that of the baseline, a sharp leading edge lips must be used. With a sharp leading edge, increases in L/D were possible. For the 12% t/c channel, a 17.2% increase was realized, as seen in Figure 19. Similarly to the rounded channel airfoils, as the channel width decreases for a sharp channel airfoil, the aerodynamic performance decreases with a drop in L/D.

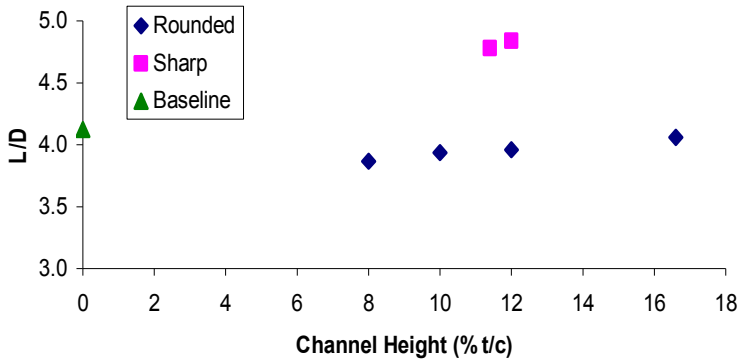

Figure 19. L/D Values for Various Configurations at M_∞= 2.5, 35,000 ft altitude, and α = 6°

Two main differences occur with the sharp leading edge compared to rounded leading edge that would change the performance of the airfoil. With the sharp leading edge, less of the airfoil chord length was cut away. The greater chord length provides a larger lifting surface during supersonic flight. The varying amounts of lift can be seen in Table 7. The largest chord length was the baseline airfoil which provided 17,805 N of lift. The rounded leading edge airfoil had the least amount of lift generated; only 15,637 N,

and it was also the shortest airfoil. The sharp leading edge was located between these two airfoils in both lift provided and also in chord length, yet it still had the same channel height as the rounded airfoil. This trend in a greater chord length providing more lift was also true for varying channel heights. With a smaller channel height, less of the airfoil was cut away. For the 8% channel only 7% was eliminated as opposed to the 16.6% where 11% was cut away. In all cases, the longer the airfoil chord, the larger the amount of lift generated.

Table 7. Summary of Forces on Airfoil Surface (N/m^2)

	Drag Force			Lift Force			
CaseName	Pressure	Viscous	Total	Pressure	Viscous	Total	L/D
cr0c12m25a6	2616	778	3394	16481	-75	16407	4.83
cr6c12m25a6	3313	620	3933	15637	-60	15578	3.96
c__m25a6	3990	321	4311	17805	-30	17775	4.12

The second main difference was the leading edge geometry. The sharpness of the leading edge as well as the height of the channel did not allow a bow shock to form over the entire front of the airfoil. Instead, two small bow shocks formed in front of each lip. This difference in the flowfield at the leading edge can be seen in Figure 20 These small shocks, coupled with the sharp leading edge which gave only a small stagnation region, caused the pressure drag to be much less than any rounded leading case. This did cause oblique shocks and expansion waves to be present in the beginning area of the channel. The large decrease in drag more than countered the smaller decrease in lift compared to the baseline airfoil and caused the 12% sharp channel airfoil to have a greater L/D, improving the overall aerodynamic performance of the airfoil.

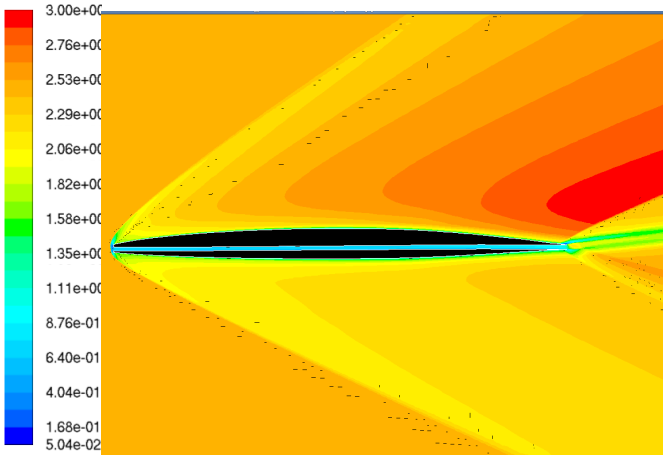

a) cr6c12m25a6

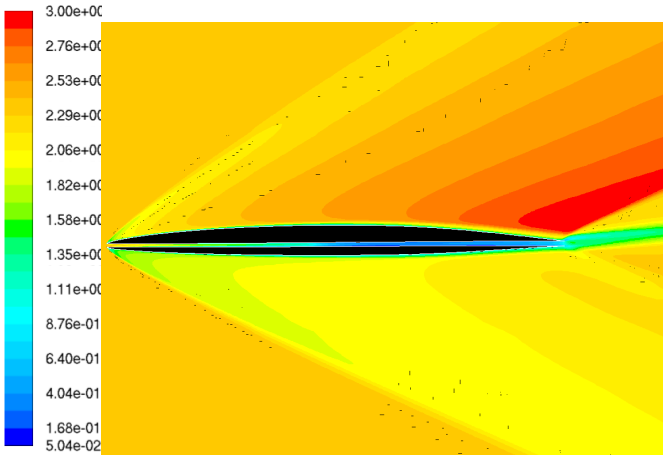

b) cr0c12m25a6

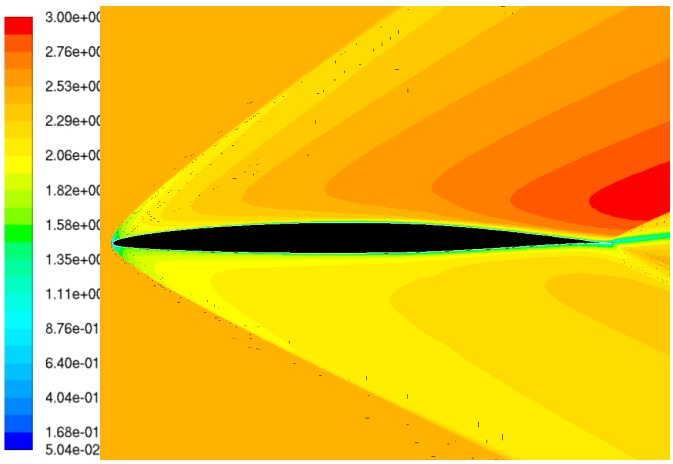

c) c____m25a6 (baseline)

Figure 20. Overall Flowfield, Contours of Mach Number

The flow field of the rounded leading edge airfoils was dominated at the leading edge by a bow shock. At the trailing, oblique shocks were also present in all cases as seen

above in Figure 20. This overall shape matched very similarly to the baseline airfoil. Despite having the channel through the whole airfoil the bow shock would still form at the front, even for the large 16.6% channel. After leaving the subsonic region at the front of the airfoil, supersonic flow over the airfoil continued to accelerate without any interruption until the trailing edge of the airfoil where it would undergo oblique shocks as three major pathways all interacted with each other.

At the trailing edge, the channel outlet and also the two surfaces came together. The top surface went through a simple oblique shock as the flow is turned from a downward direction to 6° from horizontal as seen in Figure 21. The flow was also turned because of the presence of the slower flow coming from the channel. The exit flow from the channel was sonic at the exit. As it exits, it acts as an underexpanded nozzle and expansion waves are present which accelerates the flow to over Mach 2 just outside the exit of the nozzle. This also causes the oblique shock on the upper surface to be more severe. On the lower surface, multiple flow entities were present. First the flow goes through an oblique shock as the flow turns back on itself. In the baseline airfoil, this was a simple expansion wave, but because of the expanding flow coming from the exit of the channel, the flow must first go through a shock. A short distance later, it can be seen that the flow goes through an expansion wave. This accelerates and turns the air to match the freestream flow which was at 6°.

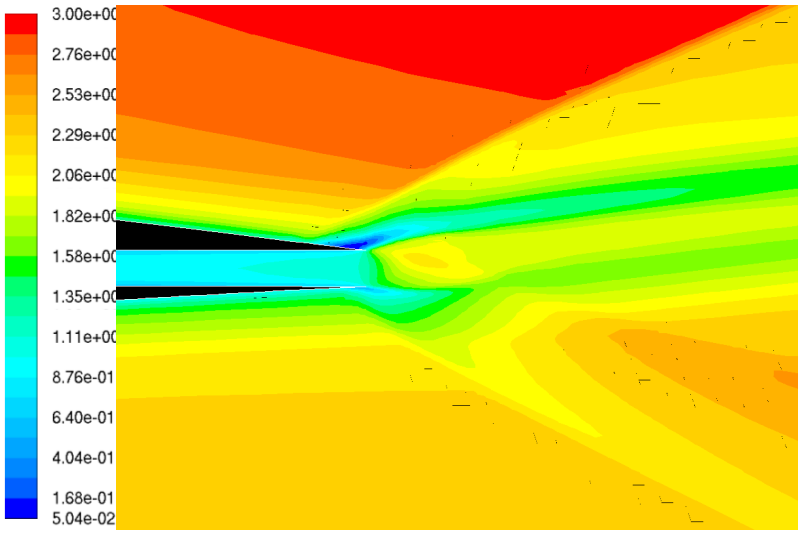

Figure 21. Trailing Edge Flowfield of cr6c12m25a6, Contours of Mach Number

A full bow shock formation was possible because the flow was choked near the trailing edge of the airfoil. This pushes the subsonic region up through the channel towards the leading edge. The two small stagnation regions on either lip form their own bow shocks. If the channel is sufficiently small, these bow shocks can interact along with the choked channel to form a continuous bow shock in front of the leading edge. This is shown in Figure 22 for the 8% channel. The two stagnation points were both located on the rounded sections of the lips of the channel. The bow shock was curved around the front of the airfoil. For larger channels, the bow shock in front of the channel has a flatter shape. This was due to the bow shock regions associated with each lip having less of an interaction, causing a weaker area directly in front of the channel. However, for each rounded case, the bow shock was still present.

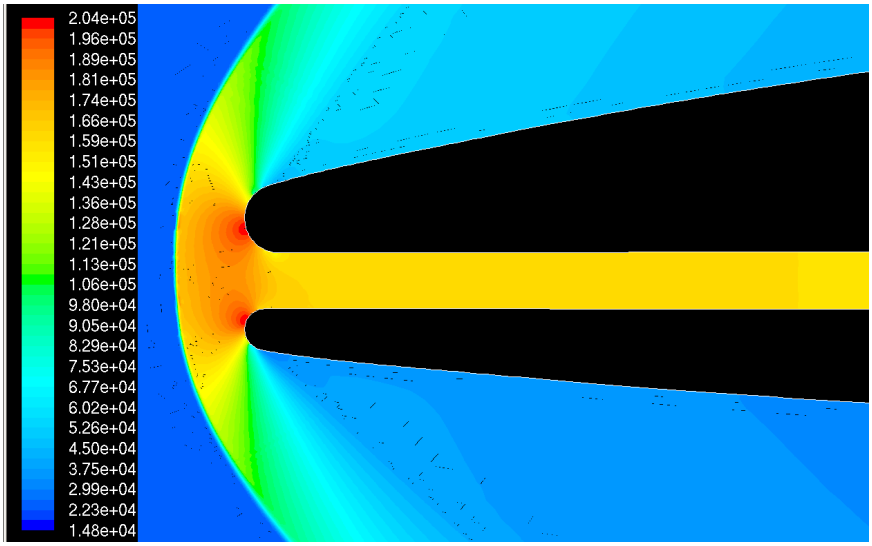

Figure 22. Leading Edge Flowfield for cr6c8m25a6, Contours of Pressure

Close observation of Figure 22 shows that the stagnation point was not directly at the point that was the most forward. After inspecting the pathlines shown in Figure 23, it can be seen that the stagnation points were both inside the channel area. For the top lip, after traveling through the bow shock, the flow turned slight and hit the went directly towards the stagnation point at the 6° angle. For the lower lip, the flow had to turn back down and the stagnation point was located at a point not directly in line with the freestream. The mass flow needed to choke the flow was able captured by a frontal area less than the width of the channel. This caused the flow to separate around the lips as shown. Because of the direction of the flow, the drag was less because of the transformation into the flow coordinates. The flow had a normal direction of 15.4° from centerline at the lower lip stagnation point. This caused only 93.1% of the force to be seen as a drag force. The remaining vector did contribute to lift loss. For the upper surface, the flow did not alter direction and 100% of the force seen at the stagnation point was counted in the drag force.

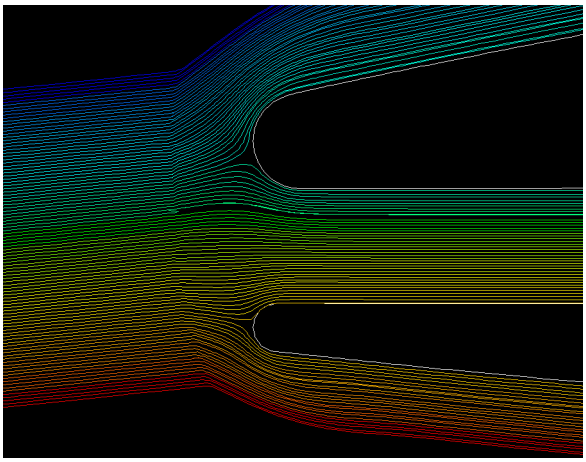

Figure 23. Leading Edge Pathlines for cr6c8m25a6

The large stagnation point on the baseline airfoil was split into two points for the channel airfoil. The magnitude of the pressure coefficient (C_p) was about 1.7 in all $M\infty$= 2.0 cases. However, the high pressure region was much smaller for the channel cases. The sharper decrease in a C_p for the channels when compared to the baseline airfoil can be seen in Figure 24. The channel design exhibits similar trends over the external surfaces of the airfoil as the baseline airfoil. No lift was produced from the channel because of the balance of the pressure forces, easily seen in the graph as the two faces are the same distribution. The irregularity for the 16.6% channel was caused by the flow starting to accelerate to sonic speeds inside of the channel. Since the flow from the channel was exiting at supersonic speeds, this changes the pressure at the trailing edge compared to the baseline airfoil which only has to match two flowfields. Small changes in the trailing edge can have a influence on the flowfield. The examination of how the shaping and size of the channel exit can effect outer and inner surface pressure distribution is a task for future study. The pressure data from inside the channel will be used in the structural analysis.

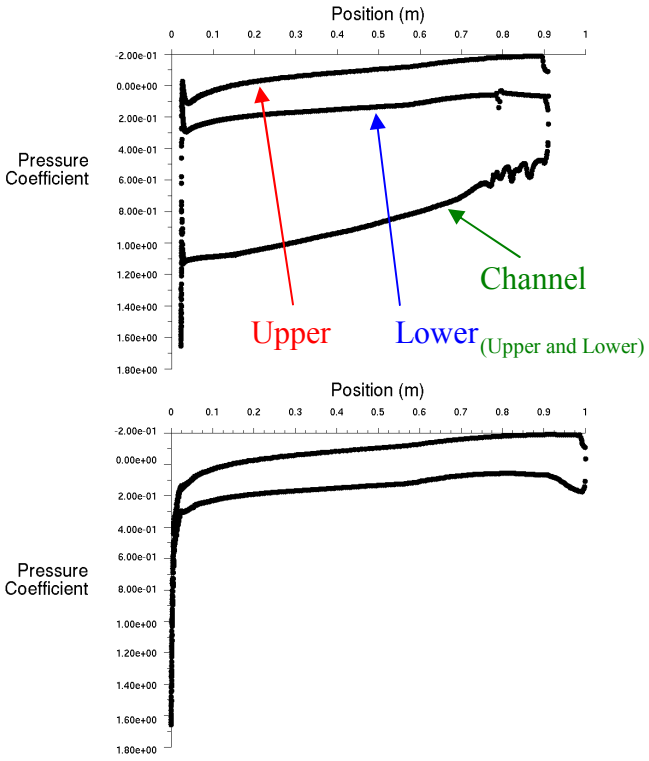

Figure 24. Pressure Coefficient Distributions on Exposed Surfaces for a) cr6c16m2a6 and b) c____m2a6

After entering the channel, the slowest part of the flow besides the boundary layer was at the narrowest part of the channel where the tangency condition of the channel and the leading edge lips were met. After this point the flow slowly accelerated despite the channel size growing. This can be seen in Figure 25 which shows all areas of the flow that were below Mach 1. The speed at the start of the channel was around Mach 0.5 but by the exit, the flow has choked and was at Mach 1. Even though the channel height grows slightly because of the 0.1° wall angle, the boundary layer slowly grows towards the middle of the channel, eventually choking the flow. The pockets at the trailing edge were locations where the flow had gone sonic within the channel. For smaller channels,

the flow would not go sonic until the very end of the channel and the pockets were not present.

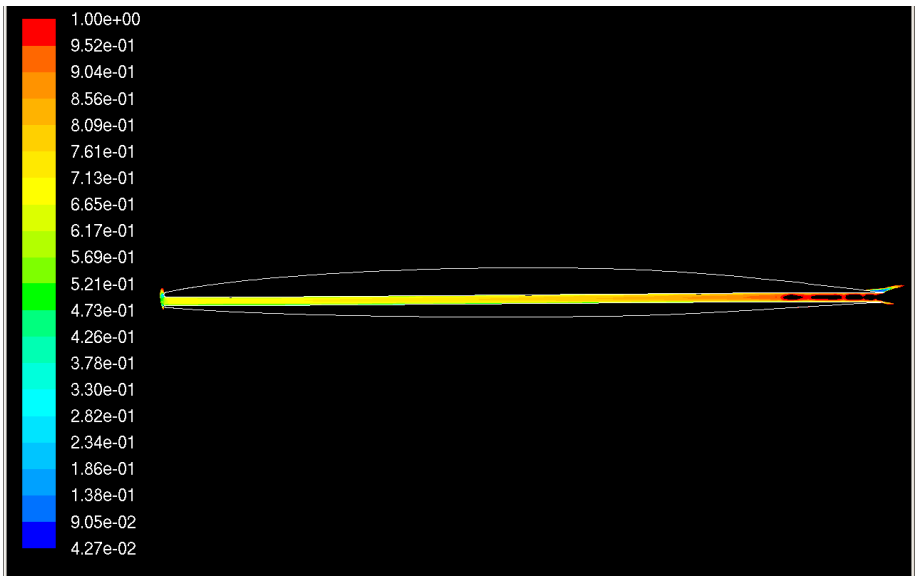

Figure 25. Channel Flowfield for cr6c12m25a6, Contours of $M_\infty < 1$

The sharp leading edge airfoil geometry provided a much different flow field at the leading edge. Figure 26 shows how the two shock regions are unable to form a continuous bow shock over the front of the channel. Instead, oblique shocks and expansion waves are present in the channel. This appears as a wave going through the channel but if further fidelity to the color scheme is used, the alternating triangular regions become clearer. These shocks and expansions work to slow the flow to subsonic within the channel, similar to a supersonic inlet. The stagnation pressure regions are much less severe than the rounded channel, and a lower wave drag is the result. The smaller frontal area of a sharp channeled airfoil reduces the total drag on the airfoil. Referring back to Table 7, the supersonic flow in the channel does increase the amount of viscous drag by 25% over the rounded leading edge geometry which contains subsonic flow throughout the entire channel. The decrease in pressure drag was only 21%.

However, at supersonic speeds, the wave drag magnitude was approximately four times greater and overall the sharp leading edge gave a 14% lower drag force despite the sonic flow present at the beginning of the channel.

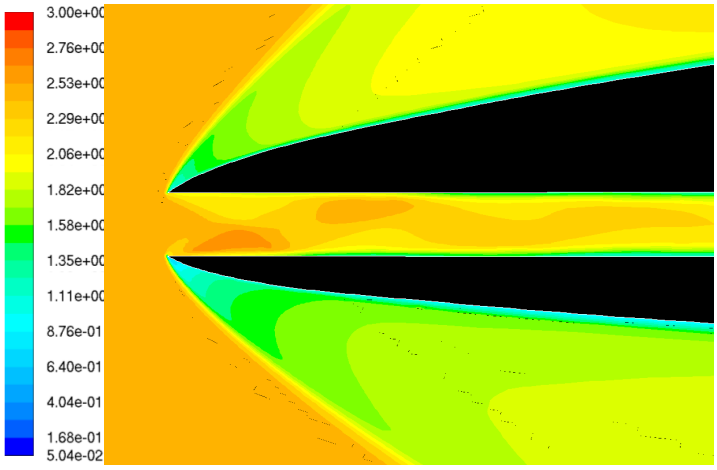

Figure 26. Leading Edge Flowfield for cr0c12m25a6, Contours of Mach Number

Despite having a much different flow field at the leading edge, the trailing edge velocity profiles were similar to the rounded leading edge profiles. The gradient of the flow from the upper surface of the airfoil to the freestream was much higher as seen in Figure 27. The oblique shock was still present and was still affected by the flow exiting the channel. The channel exit flow expanded, but the lower surface flow was not as affected. The oblique shock was weaker and was almost immediately combined with the expansion region. This was due to the lower part of the airfoil experiencing a higher speed flow. These higher speeds were possible because the large bow shock region that extends far out from the airfoil was not present. The higher energy flow could compensate more readily to the expansion area present at the trailing edge of the channel.

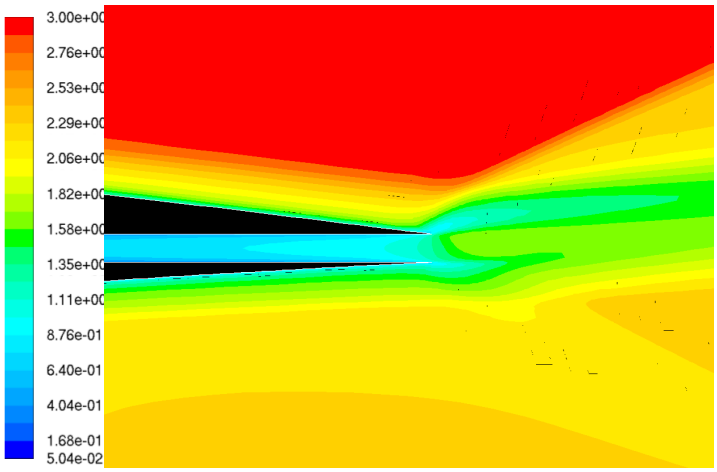

Figure 27. Trailing Edge Flowfield for cr0c12m25a6, Contours of Mach Number

The experimental space was expanded to determine if by changing the freestream Mach number that the rounded channel airfoils could have higher L/D ratios than the baseline geometry. The sharp leading airfoils were also looked at and the results are summarized in Figure 28, where S is a sharp leading edge and R is a rounded leading edge for the channel geometries. At Mach 2, the 16.6% round channel exceeded the baseline airfoil. If the freestream Mach number was decreased to 1.5, all geometries outperformed the baseline. The 16.6% channel had an increase of 3.5%. However if the speed was increase to Mach 3, the baseline once again outperformed all rounded channel airfoils. As Mach number decreased, it was seen that the amount of lift generated by a channeled airfoil was much closer to that of the baseline. At Mach 2.5, the 8% channel airfoil lost almost 10% of its lifting capability compared to that of the baseline while outperforming the baseline by about 4.2% for drag. When the same case was run at Mach 1.5, the results were a loss of only 7.4% in lift with a gain of 7.5% for drag. By traveling at a slower speed, the shape of the airfoil has more of an effect on the lifting capabilities whereas at higher speeds, the amount of lifting surface becomes the main driving factor.

The increase in drag performance was due to the viscous drag. Both cases had similar pressure drag reduction, but the slower speed caused the viscous drag only to increase by about 67% for the Mach 1.5 case instead of almost doubling at higher speeds.

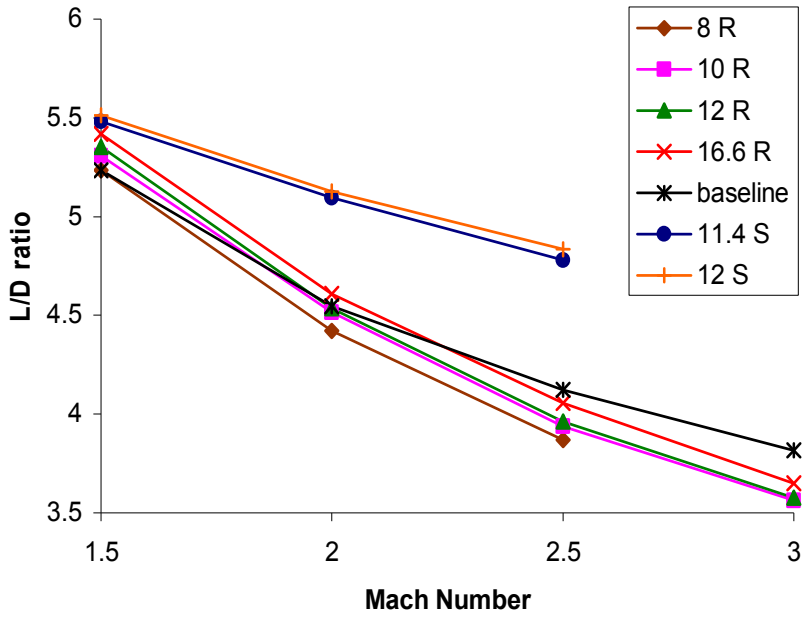

Figure 28. Computed L/D for M_∞ = 1.5 - 3.0, α = 6°

The sharp channel geometries continued to outperform the rounded channels for all Mach numbers. The advantage decreased with decreasing Mach number. The lift losses for the rounded airfoils were not as large at the lower Mach numbers. The sharp leading edge actually had a higher lift loss at Mach 1.5 than Mach 2.5 with losses at 8.8% and 7.6%, respectively. This was because there were some suction forces present and the slower Mach numbers to improve the lifting characteristics of the blunt body airfoils. Also the bow shock was not as strong causing the stagnation region to be not as severe. Thus the performance of the sharp leading edge, which had the advantage of being the best reducer of pressure drag for a given channel thickness, was inhibited and only slightly better that the rounded channel entrance airfoils.

A third study was undertaken to determine the performance of different types of channels. Besides the normal two kink channel used in all cases above, a channeled airfoil was created that started with an 8% channel at the inlet but the exit was a 16.6% channel. This gave the effect of a diverging nozzle because the expansion was much greater than the 0.1° used for a normal channel. However, since the flow exit was so much larger than the inlet, the flow did not choke at the end of the channel as seen in Figure 29. Instead the flow choked at the narrowest point of the channel, right at the inlet. This caused supersonic flow throughout the entire length of the duct. The bow shock structure correlated with a constant channel height 8% channel.

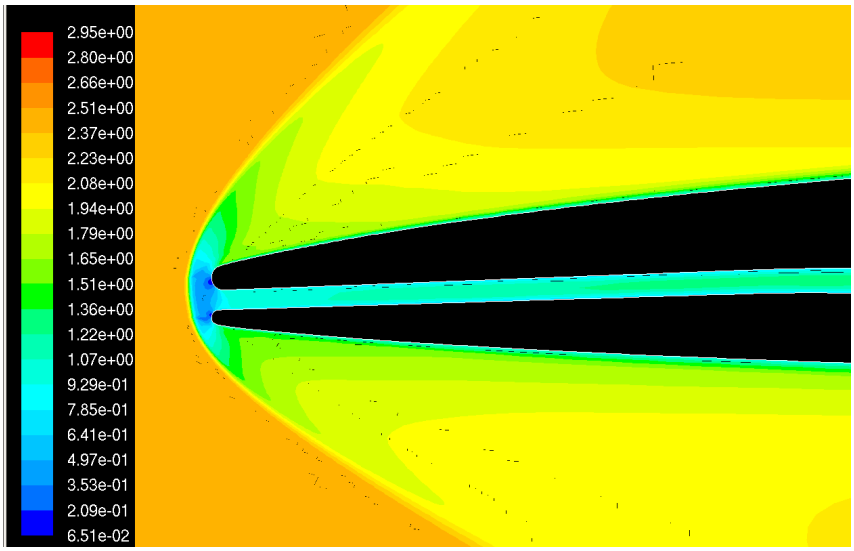

Figure 29. Leading Edge Flowfield for cr6c8_16m25a6, Contours of Mach Number

The expanding channel was designed in this manner to try and get a propulsive force out of the high pressure air in the channel, thus reducing the overall drag of the airfoil section. The channel was varied to explore how changing the channel geometry could affect this propulsive force or allow for duct flow that did not have as much drag.

The results for the straight channel and the one and two kink models can be seen in Table 8. The only change seen was at the third significant digit, and the difference in L/D was only 0.2% which could be attributed to how coarse or refined the grid was. Despite what interior channel geometry was in place, the drag forces present were approximately that of an 11% channel. The viscous drag was similar in magnitude to an 8% channel, but the pressure drag was decreased when compared to just an 8% channel. The pressure in the channel pushed on the interior walls of the channel, overcoming a portion of the stagnation pressure, making the airfoil have the same pressure drag as an 11% channel.

Table 8. Computed L/D for Altered Internal Geometries

Geometry	L/D
cr6c8_16m25a6_Str	3.843
cr6c8_16m25a6_1kink	3.838
cr6c8_16m25a6_2kink	3.847

A summary table of all two dimensional aerodynamic cases performed can be found in Appendix A.

Structural Analysis Results

The structural analysis portion determined the allowable span of the channel due to the cut needed through the spars of the aircraft. PanAir, a panel code, was used to approximate the loading the wing would incur during Mach 2.5 flight. Using the wing planform from the reference aircraft (Rinioe, Wright), the resultant lift distribution was determined using the doublet strength at the trailing edge. Given a 665,000 lb base cruise weight for the aircraft (Wright), the forces on the wing were determined. A chord length of 7.024m was determined by the halfway point of the outboard section of the cranked arrow design. This chord translated into a 0.298m high spar for the 0.15c spar. The forces

present at the end of spar width, where a rib would attach, were a moment of 14,534 Nm and a vertical point load of 2,075 N determined from the air load analysis.

Tensile yield was the failure criteria examined for the finite element analysis of the spars. The material, Aluminum 2024-T4, has a tensile yield stress limit of 3.24×10^8 Pascals. The cross section was designed to have an analytical maximum stress of the yield limit. The clean beam was placed into the finite element program and the stress distribution obtained can be seen in Figure 30. Stress was measured along the bottom flange of the I-beam. From left to right, the stress distribution describes the loads present in the beam from the fixed rib to the loaded rib part of the spar. Because of the use of solid elements, the data at the edges of the model were below that predicted analytically. A maximum of only 318 MPa was seen for the computer model and the behavior was not smooth at the boundaries. However, the area of interest was the center of beam which had regular behavior. To adjust for the discrepancy at the boundary, the failure criterion was set at 318 MPa for the computer model instead of the 324 MPa theoretical limit.

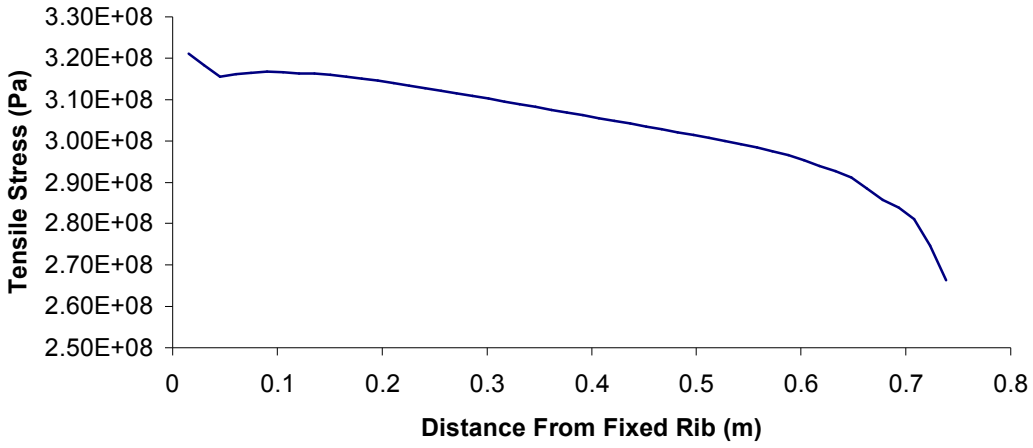

Figure 30. Stress Distribution for Baseline Beam under Resolved Load

The first channel shape examined was a circular cut with diameter of the height of the channel used in the 2D airfoil analysis. Figure 31 shows the stress distribution for the 12% cut for both the spar at 0.75c and 0.15c along the bottom flange. The 0.15c spar contained the most critical stress value of 3.23 MPa and all subsequent structural analysis used the 0.15c spar as the baseline. Even though the channel was larger for the 0.75c spar, the cutout for the 0.15c was farther away from the center of the beam. The asymmetry had a greater role in determining the stress concentrations compared to just the size of the cutout. Two stress peaks were found corresponding to either side of the cut through the spar. These were higher than the stresses observed at the boundaries, causing the critical area to shift to the middle of the beam, near the cutouts.

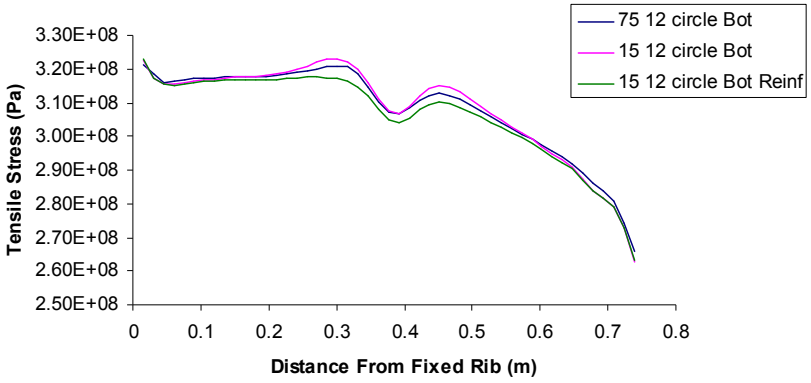

Figure 31. Stress Distribution for 12% circular channel

The third distribution shown in Figure 31 was the reinforced hole. As discussed in the Method section, the cut material was added around the hole to reinforce. This increased the moment of inertia of the cross section and lowered the stress. It also stiffens the web and allows an attachment point for any channel ducting. The maximum stress value along the bottom flange for the reinforced circular hole was 318 MPa, the allowable limit.

Another critical surface was along the inner edges of the hole itself. Stress measurements were taken around the hole starting from the point closest to the fixed rib end, then proceeded along the inner edge towards the center of the spar. The magnitude of the stresses encountered can be seen in Figure 32. The stresses from 30° to 120° were compressive stresses. The critical stress was of the tensile nature and located at the bottom of the hole, the closest location to the flange. Without reinforcing the cutout, the spar also fails in tension at the hole location. However, once the whole was reinforced, a factor of safety of 1.17 was present at the maximum stress location.

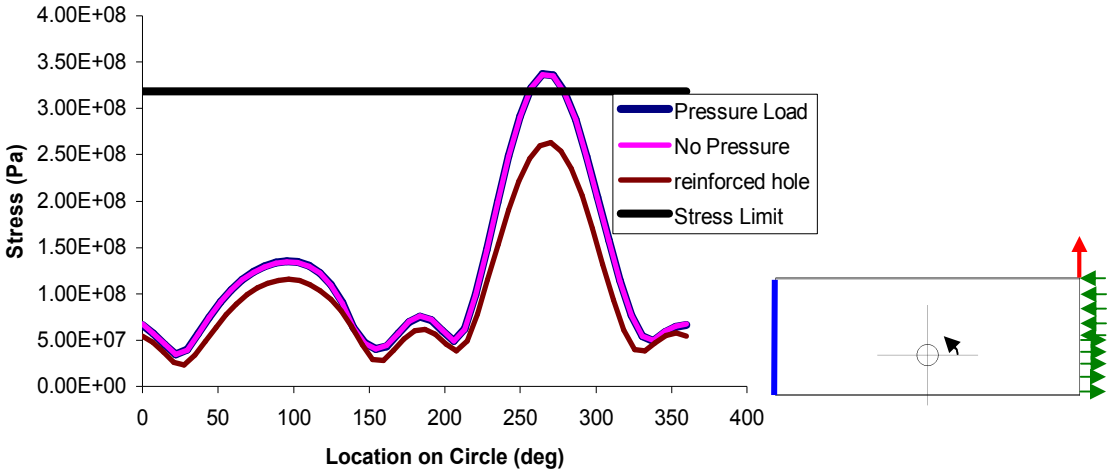

Figure 32. Stress Distribution around 12% Circular cutout

The pressure loads associated with the air traveling through the duct were considered by resolving the load to the 0.15c and 0.75c spars. This was then applied as a pressure load to the interior surface of the hole cutout. The stresses present were almost identical to having no pressure load added, as seen above in Figure 32. Reinforcing the cutout had a greater effect on the stresses. Since there was little change, the pressure load was assumed negligible for the tensile failure criteria and was not put in further analyses

for simplification. The pressure load may affect other failure modes not explored in this analysis.

Different channel heights besides the 12% channel were examined. Figure 33 summarizes the peak stresses seen on the bottom flange. The larger the hole, the stress concentration gets larger. For the 8% hole, the peak stresses were only as high as the stress seen at the boundary conditions. After 12%, a large jump was seen. As the circle diameter grows, there was less material between the hole and the flange to carry the load. At a certain point, this reduction in area causes a shift in the load path, increasing the stress peaks observed.

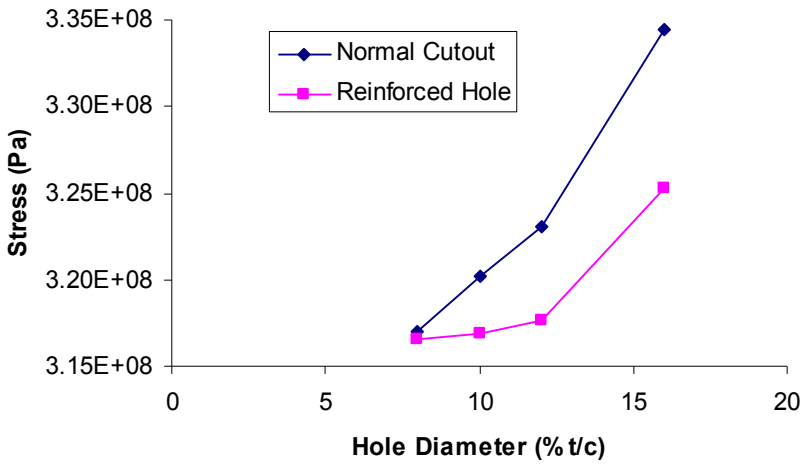

Figure 33. Stress Peaks along Bottom Flange for Circular Cutout

A square hole was also cut out of the spar. The stress distribution along the bottom flange exhibited the same trends as the circle cutout with the reinforced hole again having a maximum stress value of 318 MPa. Around the hole, the stress pattern was much different and can be seen in Figure 34. The degree locations are the same as in the circular case. Two meshes were examined for the unreinforced hole, one with a coarse mesh of about 20 nodes per each square side and another with a finer mesh with

40 nodes. With the coarse mesh, the square outperforms the circular cut by not exceeding the tensile stress limit of the material. Instead of the forces acting a single point at the bottom of the circle, the flat side of the square was able to dampen out the concentration towards the corners of the square. At the corners, the coarse mesh was still less than the tensile yield limit. When the mesh was refined to try and capture the stress concentration seen in the coarse mesh more accurately, the expected behavior of the square appears. The sharp corners become large stress concentrations, exceeding the tensile yield limit. With further refinement, the stress would be expected to continue to increase because of the discontinuities associated with a square type cut. An interesting observation was that the largest concentration was at the 225° point. This was on the side closer to that of the loading which, for the flange area, typically experienced a lower amount of stress. Since the beam was bending upward, the 225° corner was where the load path first interacts with the hole, which could cause this point to have a larger stress value.

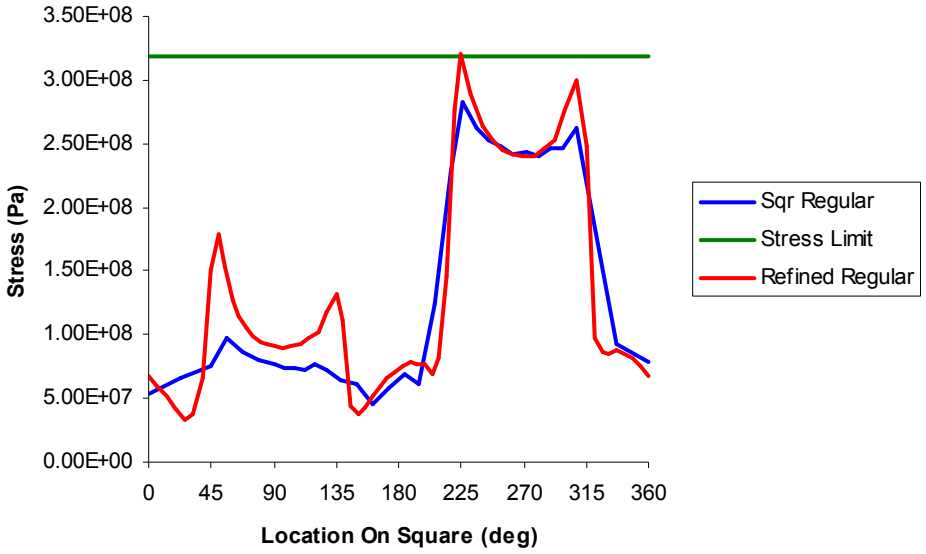

Figure 34. Stress Distribution around 12% Square Cutout

The slot geometries for the 12% channel were also examined using the techniques above. The peaks along flange continued to spread towards the ends the larger the slot was made. The peak value was always on the bottom flange on the side of the fixed rib, the maximum measured value being 350 MPa for the unreinforced 50% wide slot. A summary of these peak stresses are tabulated in Table 9. All slots failed the tensile yield maximum allowable. As the slots grew wider, the amount of the beam with stress levels above the maximum allowable was larger. Once the holes were reinforced, the stresses were much closer to the limit. Even at 50% of the spar width, the peak stress on the bottom flange was only 3.5% above the 318 MPa limit. The sharp concentrations visible on the inside surfaces in the square cutout were not present for the slot geometry. The flat surfaces of the slot exhibited the same lower stress value as in the square. The continuous corners leading into the half-circle portion of the slot dampened out the sharp stress concentrations seen in the square geometry into smooth rises. The maximum stress on the inner face of the slots was always less than that of the peak bending stress on the bottom flange surface.

Table 9. Stress Peaks along Bottom Flange for Slotted Cutout

Slot Size	Normal Cutout (MPa)	Reinforced Hole (MPa)
Square	330	322
25%	342	327
50%	350	329

In order to take most advantage of the aerodynamic benefit of the channel airfoil, the 0.15c spar, 12% channel with a 50% width cutout was analyzed further. The stress distribution was examined and it was seen that the maximum stress for both the normal cutout and the reinforced slot was on the side nearest to the fixed end. The stress peak on

the loaded end side for the reinforced beam was lower than the maximum tensile yield stress of the material with a value of 306 MPa, as seen in Figure 1. The lower flange was tapered by taking material from the loaded end and added to the other side. The tapering values were set to lower the fixed end stress peak down to 318 MPa. When the fixed end side had been optimized for 318 MPa, the loaded end was above the yield stress by 2 MPa (320 MPa). This showed that with a 12% channel, and a 50% width, the structure would not be able to pass the tensile yield failure criteria. The final taper dimensions were .127 m for the loaded end flange width which linearly grew to 0.303 m for the fixed end.

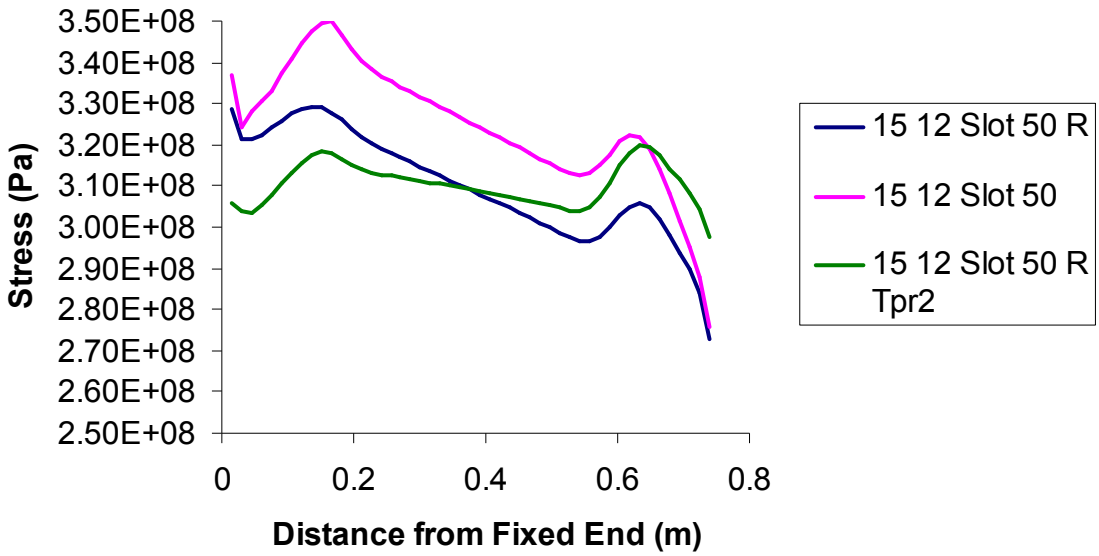

Figure 35. Stress Distribution along Bottom Flange for 12% Channel Height, 50% Slotted Width Cutout

In order to meet the tensile failure criteria, the slot size was reduced to 10%. After the tapering principles had been applied, this was found to be a conservative design with maximum stress peaks of 318 and 314 MPa for the fixed and loaded ends, respectively. This data, coupled with the 12% channel data, determined a design solution of 11.4.

Table 10 shows the peak stress results for each of the 0.15c spars with the 50% slot channel. Only one 11.4% model was constructed as a check that the interpolation schemes gave the correct sizing for the beam. The sizing was as it should be and both peaks had stress values of 318 MPa, the imposed limit on the material.

Table 10. Slot Sizing and Peak Stress for Reinforced 50% Slot Geometry

Slot Size	Initial Flange Width (m)	Loaded End Peak Stress (MPa)	Fixed End Peak Stress (MPa)
Square	330	322	322
25%	342	327	327
50%	350	329	329

The stress distribution for the 11.4% channel beam had two stress peaks; both at 318 MPa as seen in Figure 36. In the center of the beam, the stress increased linearly the closer to the fixed end the stress was measured. As in previous models, the size of the solid cells at the application of the boundary conditions and loading caused irregularities in the data at the two ends. However, the data in the areas of interest showed smooth trends and a lack of sharp stress concentrations. With tensile yielding as the failure criteria, an 11.4% channel over 50% of the span between two ribs and a circular close out of the channel will have a factor of safety of 1.0. The final configuration can be seen in Figure 37.

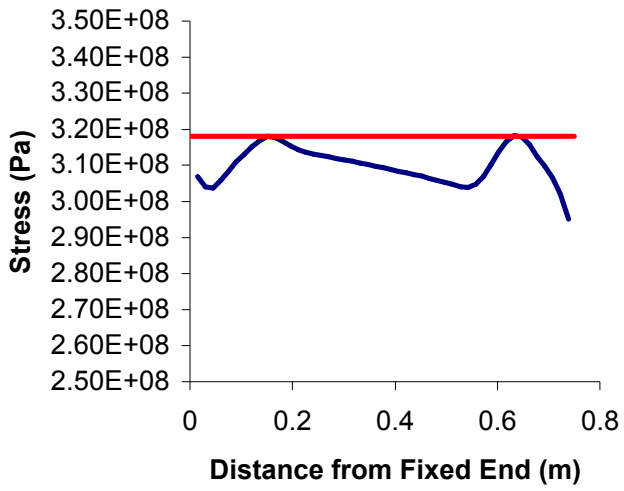

Figure 36. Stress Distribution along Bottom Flange for 11.4% Height, 50% Slot Width with Reinforced Cutout and Tapered Flange

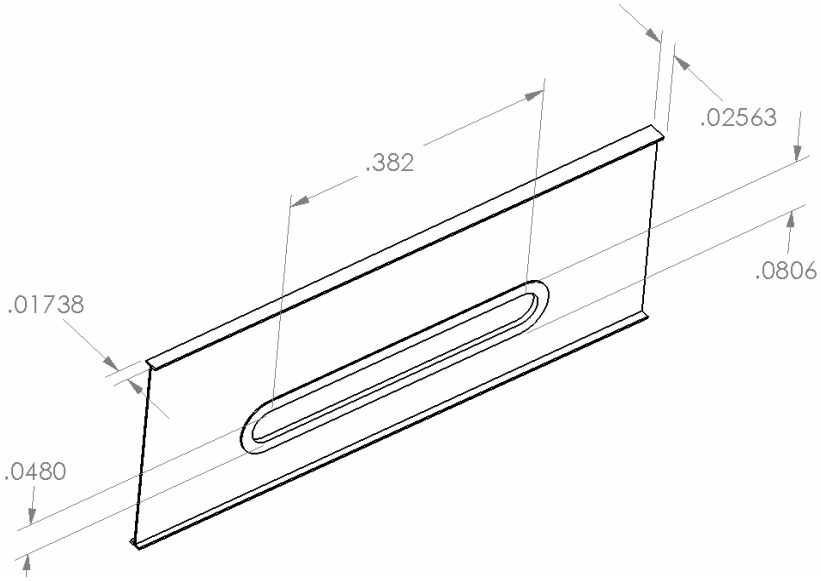

Figure 37. Configuration of 11.4% Height, 50% Slot Width with Reinforced Cutout and Tapered Flange (m)

A summary table of all structural cases run can be found in Appendix B.

3D results

A three dimensional model of a representative section of the wing was analyzed at Mach 2.5, a standard altitude of 35,000 feet, and a six degree angle of attack. The chord length was one, identical to the two dimensional model. Instead of infinite span, the span was set at .764c. The boundary conditions were symmetric and there was no sweep introduced in the wing. This simulates an infinite wing and the performance characteristics of the three dimensional model should be equivalent to that of the airfoil section. A summary of the results can be seen in Table 11. The difference in forces was from the different references areas that were used. However, the L/D comparison shows equally dimensionalized results. The L/D of 4.102 for the baseline wing model was slightly less than the infinite airfoil section model which gave a result of 4.123 for the same conditions. The small difference in the overall result gives confidence to the 3D model and validates the conversion from 2D to 3D mesh.

Table 11. Forces on Baseline Model for 3D (N) and 2D (N/m^2)

	Drag			Lift			
	Drag Force			Lift Force			
CaseName	Pressure	Viscous	Total	Pressure	Viscous	Total	L/D
Baseline 3D	436	36	472	1941	-3	1938	4.106
c__m25a6	3990	321	4311	17805	-30	17775	4.123

The results were similar as the grids for the three dimensional case were seeded the same as the two dimensional case. When using hex elements, the computations are different than when using a quad element which contributed to the differences. The capture of the bow shock and the boundary layer may have differed with the more complex three dimensional elements, contributing to the variation between the two cases.

An overall view of the flowfield can be seen in Figure 38, which shows a typical cross section of the three dimensional case. The shape of the flow field and the elements directly match the flowfield of the two dimensional case. This was expected because the .764c model simulates an infinite span wing of which the two dimensional model is an exact solution.

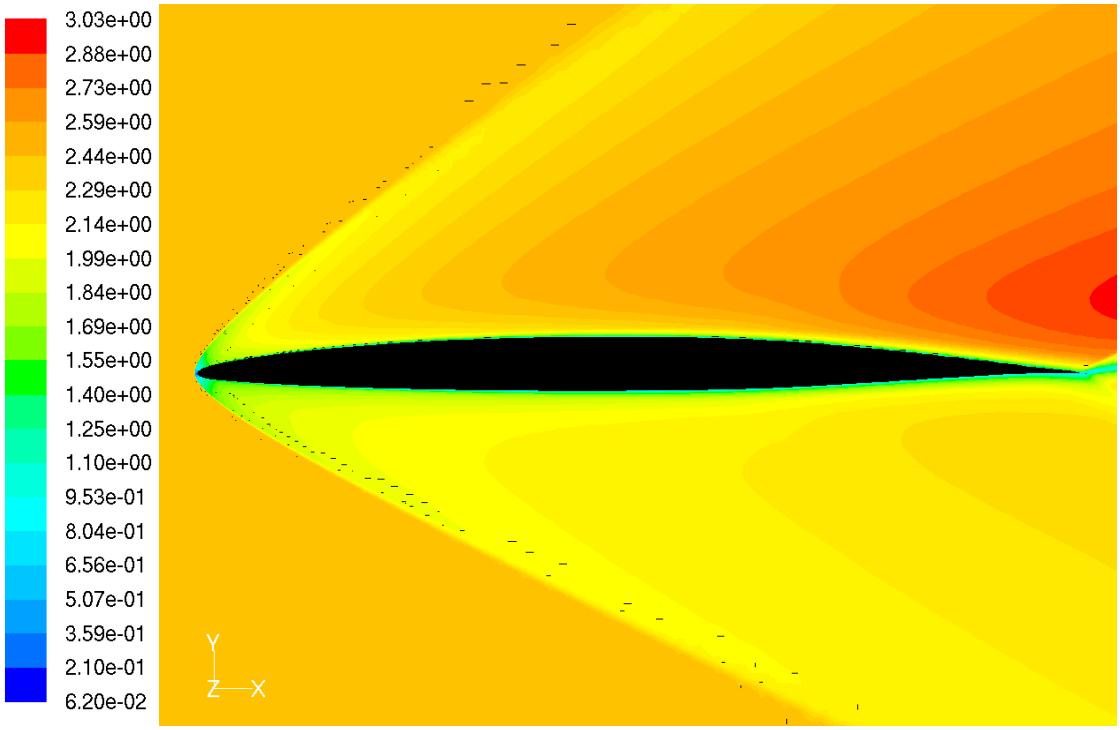

Figure 38. Section View of 3D wing at Mach 2.5, 35,000 ft, $\alpha = 6°$, Contours of Mach number

After the baseline model had been created, the slotted three dimensional model was examined. With the same boundary conditions and farfield settings, the slotted model showed an L/D improvement of 9.2% over the baseline model with an L/D of 4.48 as shown in Table 12. In the table, the forces on the slotted wing geometry were doubled since the computation was performed on a half model. The drag force was reduced by 64 N and the lift force was decreased by 108 N. The reduction in lift was followed what had

been seen in the 2D airfoil section analysis. The lift reduction was 5.5% for the entire model. This was similar to the 11.4% section airfoil which had a reduction of 6.9%. The discrepancy was expected because some of the slotted wing was not altered and had a full airfoil section and thus some of the lift force was recovered when compared to a fully slotted wing.

The two dimensional baseline results were also scaled based on the 3D baseline model which had a width of .109c. For a fully slotted wing, the expected L/D value was 4.78 and using the baseline wing model, 4.102. The slotted wing had a performance that was 56% of this range even though the slot was only 50% of the wing. This increase is reasonable since the total slot did not only cover 50% of the wing leading edge. The circular close off of the slot went beyond the 50% slot allotment. This extra cutout was included in the structural model previously. This extra frontal area reduced the drag further since the channel was open to more of the span. The amount of benefit was reduced when compared to an 11.4% slot extended because the diminishing size of the close off. The benefit was not large but was apparent.

Table 12. Forces on Baseline and Channel Airfoils and Wings for Mach 2.5, 35,000 ft, α = 6°, Data Scaled to Baseline 3D model

	Drag Force (N)			Lift Force (N)			
CaseName	Pressure	Viscous	Total	Pressure	Viscous	Total	L/D
Baseline 3D	436	36	472	1941	-3	1938	4.102
50% Slot 3D	175	29	204	916	-3	914	4.480
Cr0c114m25a6	297	80	376	1806	-8	1799	4.785
naca_m25a6	434	35	469	1937	-3	1933	4.122

The external surfaces of the leading edge affected the performance of the airfoil downstream. A pressure plot of the leading edge can be seen in Figure 39. Because of the characteristics of supersonic flow three regions were formed. Near the leading edge, the

flow over the full airfoil section was the same as the 2D baseline airfoil as seen by the large stagnation region. In contrast, the slotted section of the wing had a much smaller stagnation region, similar to the 2D channeled airfoil. Where the slot section ends, the third region developed which was the interaction of these two leading edge flow features that propagated downstream. At the close out, there was no longer a surface to support the bow shock flow feature and the flow collapsed into the channel. The interaction is seen on the lips of the channel. For most of the leading edge of the slot, the stagnation region was small and was parallel to the leading edge. At the point where the bow shock at the edge of the channel close out interacted with the lips of the slot, a high pressure region developed. Also interacting at this point was the shock that was developed by the sharp edged lips of the channel itself. From this region, the propagation of a shock wave caused by this discontinuity continued along the surface of the wing, interacting with the accelerating flow over the top of the wing. The propagation of the discontinuity can also be seen on the interior surfaces of the channel.

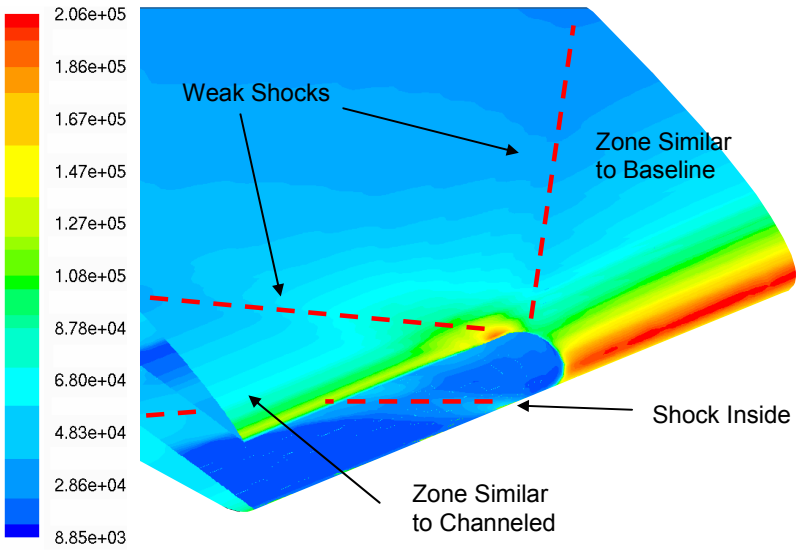

Figure 39. Pressure Contours (Pa) of Leading Edge Surfaces for 11.4% Channel, 50% width at Mach 2.5, 35,000 ft, $\alpha = 6°$

The flowfield varied for the slotted wing depending on the span location. Figure 40 shows the flowfield along the slot symmetry line. Overall, the flow characteristics were similar to that of the airfoil section with an 11.4% channel. Leading edge shocks form at the lips of the channel and the bow shock region was not formed as expected. The trailing edge also was similar, with the flow expanding out the exit of the channel and accelerating past sonic. However, because of the finite nature of the slot other elements came into play. Instead of a continuous acceleration over the upper surface, the flow was interrupted by the shock formed by the discontinuity interacting with the accelerating flow over the top of the wing. The disturbances grew weaker towards the trailing edge of the airfoil as the accelerating flow dampened out the effects of the shock. The formation of this shock and its interaction along the symmetric boundary contributed to the drag seen by the wing.

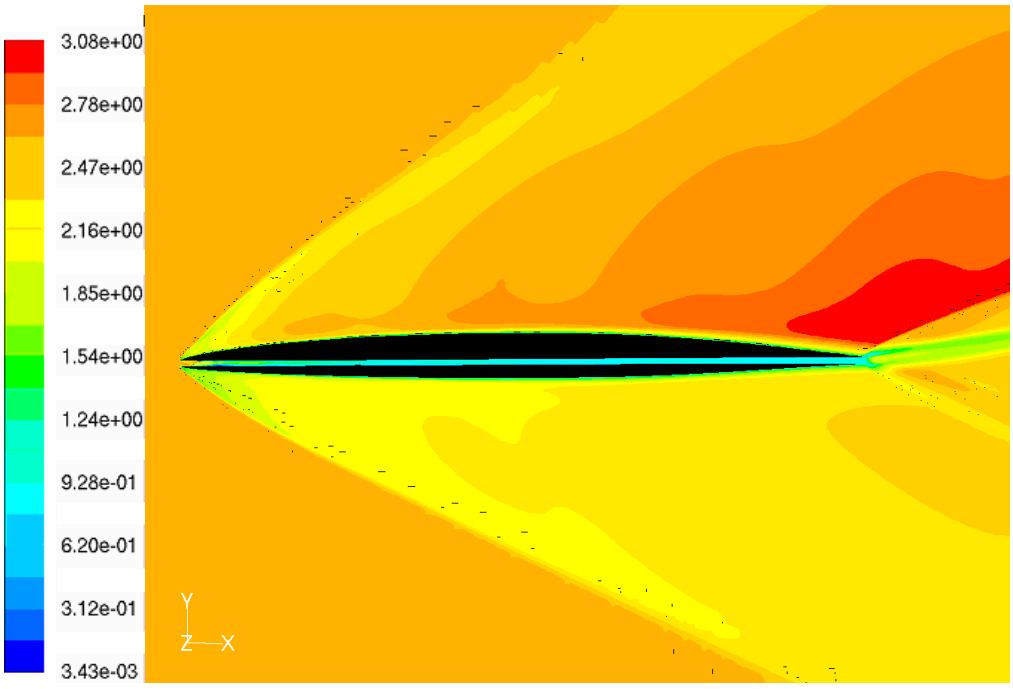

Figure 40. Mach Contours for Mid-Plane Section of 3D 11.4% Channel

The overall flow through the channel was comparable to the basic channel airfoil. Because of the boundary conditions present, the flow field was altered from the infinite channel. The centerline of the channel coincided closely to that of the slotted airfoil section model. Near the leading edge, a supersonic zone was found with both expansion waves and oblique shocks interacting. The zone eventually coalesced and became a subsonic flow at about 0.25c as seen in Figure 41. The flow stayed near sonic until the trailing edge, where the flow sped up back to supersonic speeds at the exit of the channel. Near the slot close out boundary, the flow did differ from the performance seen in the 11.4% slotted airfoil. At the leading edge, the discontinuity caused by the closeout of the slotted propagated a shock into the channel as well as the upper and lower surfaces of the airfoil. The initial region of the channel is highly convoluted as shocks generated from the upper and lower lips as well as the close out regions all interact. At about 0.05c from the leading edge, the boundary layer, which had been attached, was tripped by a wave hitting the sides of the slot. A separated region was developed after this perturbation of the boundary layer. Further down the slot, the flow became more uniform and the separation region was damped out. Since the inviscid region of the channel was smaller than usual in the front, the flow was able to expand more in the aft region of the channel. This allowed the flow to be slower in this section, only Mach 0.7, whereas in the infinite channel, the flow was near sonic or parts of the flow were expanding past Mach 1. This lower velocity allowed for less viscous drag in this part of the channel compared to the two dimensional model. This offset the drag increase caused by the separation region near the front of the channel. At the exit of the channel, the choked flow expanded and accelerated, similarly to that of the two dimensional model. The interaction of the

channel and the trailing edge portion of the airfoil had no large irregularities except oblique shocks and expansion waves to match the flow from both external and internal surfaces which was similar to that in the two dimensional analysis.

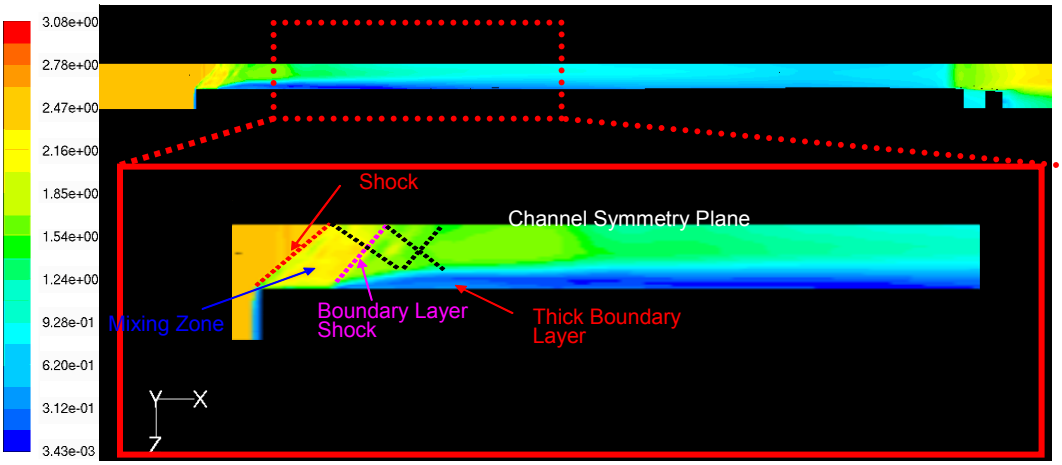

Figure 41. Mid-plane of 50% Slotted Wing, Contours of Mach number

The trailing edge of the wing was also examined. A pressure distribution can be seen in Figure 42. No stagnation points were present at the trailing edge so the static pressure was low over the region. The interaction between the close out of the slot and the wing did cause a discontinuity. The sonic flow present just at the trailing edge of the channel expanded over the edge of the wing to match the flow over the top of the wing. The singular cells that have a higher pressure were in the zone where the flow was accelerating. Because of the interactions between the boundary layer and the expansion waves, the display of the pressure profile was limited by the computer program used. Despite the graphical error, the general trend of the profile can be seen. The flow from the channel expanded upon exit of the slot. The location of the oblique shock that turns

the flow was not at the trailing edge but slightly upstream because of the influence of the expanding flow at the slot exit.

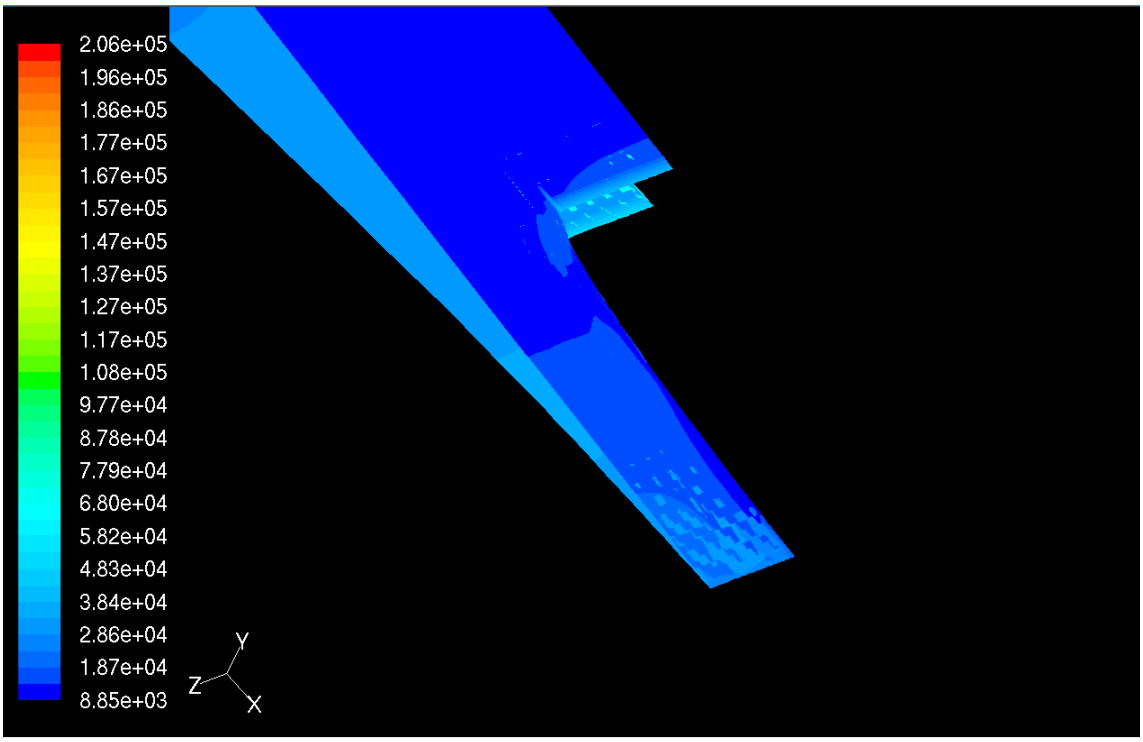

Figure 42. Trailing Edge of 11.4% Channel Wing, Contours of Pressure (Pa)

CHAPTER 4

Overall Discussion & Future Work

The initial two dimensional analysis gave insight into how the concept of a supersonic channel airfoil could be applied to a generic cambered airfoil. Initial efforts to improve the airfoil by using rounded leading edges showed some improvement with large channel heights. The rounded leading edges were initially used because of concerns of heat transfer. At hypersonic speeds, the rounding of sharp edges is required to inhibit aerodynamic heating. However, at the low supersonic speeds, the heat transfer benefit of the rounded leading edge is negligible. By switching to a sharp leading edge, two benefits were seen. First, the sharp leading edge gave better shock performance. The sharp leading edge allows weaker oblique shocks to be formed than the detached normal shock formed at the channel entrance for a rounded channel. The second benefit was that more of the chord length was recovered. When the rounded channel airfoils were analyzed, the amount of lift was much lower than that of the baseline airfoil at supersonic speeds. From thin airfoil theory, the amount of lift at Mach numbers greater than one is dependent on the length of the chord of the airfoil. When the sharp airfoil was used, less of the chord was removed and the amount of lift produced increased.

The implementation of the channel airfoil is another issue that needs further research. The current design idea is for some sort of retracting device that can be applied to the airfoil and allow the full baseline airfoil profile to be in the flowfield during subsonic maneuvers. However, if a retraction device cannot be used, the sharp leading edges of the channel will have lower performance at the subsonic speeds. The rounded

leading edge channel may be a better design for this scenario. In either case, further research into the design and implementation of the channel airfoil system is needed.

The same can be seen for the trailing edge. When the channel was implemented, most of the chord length was removed from the trailing edge because of the long thin nature of the airfoil. The current design idea calls for a retractable trailing edge but this removes 8-10% of the chord, lowering lift at supersonic speeds. Another design that could be considered would be a split trailing edge that rotates into a horizontal position, opening the channel at the trailing edge. This would increase the chord length over the previous design. There may be benefits in a three dimensional wing because the wing would no longer have a large chunk missing at the trailing edge.

The structural analysis portion of this investigation showed that a 50% slot with circular close outs at either end could provide a solution that would not add weight to a basic beam. This was if the height of the slot was 11.4% of the maximum t/c. However, the initial model used was not an optimal design to begin with. The simplified beam was used in order to see if the beam could be manipulated to give a valid result. An already tapered beam may allow for less modification and the size of the channel may need to be reduced. Other structural losses that need be considered in future research include how the duct that creates the channel will be implemented. The addition of the extra structural equipment weight and complexity for the suggested retraction devices, the duct, and any other required structure for this system may overcome any aerodynamic gain. The balance between these two competing systems needs more detailed development in future studies. Also implications of the sharp leading edge can be examined. Sharp leading edges are difficult to maintain and manufacture, however the sharp leading edge for the

channeled airfoil is rounded on one side. The limitation of how sharp the leading edge can actually be while still supporting the internal loading of the channel manufactured should be investigated.

The failure mode used was tensile yielding. Other failure modes were not considered because of the simple model used. Other failure modes are possible and may be more constraining. This may include buckling, either from the exterior forces or from the internal pressure. Another important failure mode is fatigue. Thirdly, the effects of having a channel through the wing on the aeroelastic modes of the overall wing present a wide area of future research. The interior loading of the channel could also contribute to the dynamics of the wing, especially in the beginning sections of the channel where there are shocks present. The internal pressure did not affect the tensile failure mode. The pressure would contribute to the duct design and material used. With the subsonic flow throughout the channel for a rounded leading edge channel, the duct would need a simpler design than the sharp leading edge. This is especially apparent near the leading edge, where the started inlet condition for the sharp airfoil causes shocks to be present inside the duct. In order to truly implement this system, the structural implications need to be expanded from this initial effort.

Coupled with the structural analysis, the two dimensional flow analysis provided a design solution to be analyzed in an applied wing configuration. The 11.4% slot covering 50% of the wing performed slightly better than the original prediction of a performance that was halfway between that of the baseline airfoil and an infinite 11.4% channel wing. This warrants further research that a slotted geometry may have some benefit to the lift experienced by the airfoil. Because only one slotted wing geometry was

constructed, the amount of data is limited. Further refinement and analysis of the leading edge interactions could give more insight. In subsequent research, a small study of just the frontal area may allow even further performance enhancement in supersonic flow. At the trailing edge, more refinement to the design is needed. With other trailing edge designs, the overall performance could be improved, as mentioned above in the two dimensional discussion.

In this research effort, a simple straight wing was used. However, airplane wings, especially those for supersonic aircraft, have a sweep angle associated with them. The reference airplane had two sweep angles. The initial goal of this research was to incorporate sweep into the three dimensional model. However, the focus was changed because a baseline improvement was desired to be attained. In further study, a sweep angle should be incorporated. The effects of the slot will differ in a swept wing model, and careful design will be required. Also, consideration of the boundary conditions will be needed because an infinitely swept wing will not have a symmetric condition at each span location like that of an infinitely rectangular wing. Another large area for research is other airfoils. Initial data was only acquired for three airfoils and extensive research was only done on one. Now that the benefit of a supersonic channel has been established in a cambered airfoil and not just a blunted diamond airfoil, further research into other potential airfoils may find a more suitable host for this technology. One family of airfoils that could be examined is the “peaky” airfoils. These transonic airfoils were the precursor to the “supercritical” airfoils and achieve transonic performance by having the minimum pressure point near the leading edge. This causes the pressure rise to be more favorable along the length of the airfoil, and reduces separation caused by shock and boundary

layer interaction (Smetana). These airfoils do not have a cusp in the aft section and this could help eliminate the need for kinking the duct through the airfoil. A typical peaky airfoil, nlr1, is shown in Figure 43 (UIUC database).

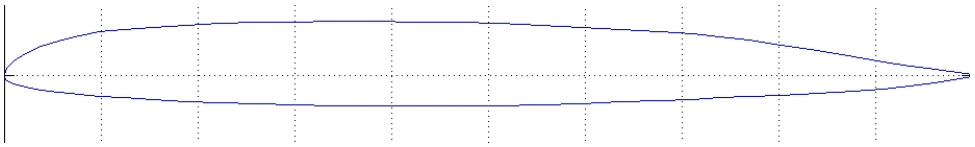

Figure 43. NLR1 Peaky Airfoil Profile

Change in the configuration of the slot may also be beneficial towards the effectiveness of this concept. The current spar configuration limits the airflow at the 0.15c and 0.75c locations. This may allow the slot to be 60% or more at the leading edge and taper back to the 50% at the spar locations. By contouring the inner slot geometry to the Mach angle, more aerodynamic benefit may be see with little structural penalty. Also the slot may not need to cover the entire span in order to be effective. By carefully placing the slot, the vortices and disturbances caused by the slot closeout may interact and cause a boost in performance (Wood). This positive vortex-interference would require fewer slots. This would decrease the structural penalty caused by having many ducts go through the center of the wing and allow implementation of the concept in a few critical areas with widespread benefit.

CHAPTER 5

Conclusion

The supersonic channel airfoil concept was applied to an airfoil that was not solely designed for supersonic cruise, specifically a NACA 66-206 airfoil. Initial two dimensional results showed an increase in L/D for the airfoil with the supersonic channel implemented. The structural implications were also examined. It was found that a baseline beam could be altered to accommodate a 50% slot through the spar. The failure mode of tensile yielding was not affected by the internal pressure of the air flowing through the channel. Finally, an aerodynamic analysis of the wing structure was performed. The experiment showed an increase in the L/D of 9% for a wing with an 11.4% t/c supersonic channel height implemented over 50% of the span between two ribs. The wing examined was an infinite rectangular wing subject to conditions at Mach 2.5 at six degrees angle of attack and placed in the standard altitude conditions of 35,000 ft.

This basic enhancement of the wing can be applied in many ways. The most basic is a straight implementation into a current design wing profile would allow a higher L/D of the aircraft to occur. Another application is the reduction of the sweep to make the L/D performance with the supersonic channel to be the same as the baseline wing footprint. The reduction in sweep will allow for greater performance for subsonic operations. In either case, the application of the supersonic channel airfoil design will provide a means to decrease fuel costs, increase range, and increase payload while not compromising the subsonic performance of the aircraft.

BIBLIOGRAPHY

ABAQUS, Ver. 6.6, Dassault Systemes, 2006

Abbot, Ira H., Von Doenhoff, Albert E., Theory of Wing Sections, Dover Publications, Inc, New York, 1959.

"Aluminum 2024-T4", http://www.matweb.com, May 2007.

Anderson, John D., Modern Compressible Flow 3rd edition, McGraw Hill, Boston, 2003.

Beer, Ferdinand P., Johnston, Jr, E. Russell, DeWolf, John T., Mechanics of Materials, 3rd Edition, 2002, pp.747.

Fluent, Ver. 6.2.16, Fluent, Inc, 2005.

GAMBIT, Ver. 2.2.30, Fluent, Inc, 2006.

Gupta, A, and Ruffin S., "Aerothermodynamic Performance Enhancement of Sphere-Cones Using the Artificially Blunted Leading-Edge Concept," Journal of Spacecraft and Rockets, Vol. 37, No. 2, Mar. 2000, pp. 235-241.

Gupta, A, and Ruffin S., "Optimal Artificially Blunted Leading-Edge Airfoils for Enhanced Aerothermodynamic Performance," Journal of Spacecraft and Rockets, Vol. 36, No. 4, Jul. 1999, pp. 499-506.

Matlab, Ver. 7.0.1, The Mathworks, 2004

"naca66206.dat", http://www.ae.uiuc.edu/m-selig/ads/coord_database.html, University of Illinois Urbana-Champaign, Nov. 2006.

PanAir, 1992

Rinoie, K., and Miyata, K., "Studies on Vortex Flaps with Rounded Leading Edges for Supersonic Transport Configuration," Journal of Aircraft, Vol. 41, No. 4, Jul. 2004, pg 830.

Ruffin, S., and Gupta, A., "Supersonic Channel Airfoils for Reduced Drag," AIAA Paper 97-0517, Jan. 1997.

Ruffin, S., Gupta, A., and Marshall, D., "Supersonic Channel Airfoils for Reduced Drag," AIAA Journal, Vol. 38, No. 3, 2000, pp. 480-486.

Smetana, Frederick, Flight Vehicle Performance and Vehicle Control, http://books.google.com/books?id=8SBbA_jW3SkC&dq, August 2008

Solidworks, ver. 6, Dassault Systemes, 2004

Tannehill, John C., Anderson, Dale A., and Pletcher, Richard H., Computational Fluid Mechanics and Heat Transfer, 2nd Edition, Taylor & Francis, Philadelphia, 1997.

White, Frank M., Viscous Fluid Flow, 3rd edition, McGraw Hill, Boston, 2006.

Wood, Richard M., Wilcox, Floyd J. Jr., Bauer, Steven X.S., and Allen, Jerry M, "Vortex Flows at Supersonic Speed", NASA/TP-2073-211950, http://techreports.larc.nasa.gov, Mar. 2003 accessed Feb 2008,

Wright, B. R., Bruckman, F., and Radovcich, N.A., "Arrow Wings for Supersonic Cruise Aircraft," Journal of Aircraft, Vol. 15, No. 12, Dec. 1978, pp. 829-836.

APPENDIX A

Two Dimensional Aerodynamic Analysis Results

		DragData (N/m^2)					
CaseName	Description	Pressure	Viscous	Total	Pressure	Viscous	Total
Airfoilkwdone	20714 airfoil no channel	12238.366	332.87043	12571.236	0.1174066	0.00319344	0.1206041
br6c8_1tan	20714 airfoil with channel	10566.198	607.96342	11174.161	0.10136846	0.005832591	0.10720105
Naca 66-206	Mach 0.2	2.7143676	19.265495	21.979863	9.57E-004	6.80E-003	7.53E-003
Cr6c8m25a0		2016.3596	622.81709	2639.1767	0.019344258	0.005975092	0.02531935
Cr6c12m25a3	[.998 , .052]	2119.6386	625.38201	2745.0206	0.020335081	0.005999699	0.02633478
Cr6c12m3a0		2512.566	815.92601	3328.492	0.016739369	0.005435912	0.02217528
Cr6c12m2a0		1259.7156	435.52925	1695.2448	0.018883245	0.006528621	0.025411866
naca_m3a0		3058.1986	422.64274	3480.8413	0.020374515	0.002815756	0.023190271
Cr6c12m2a6		2549.2685	425.11874	2974.3872	0.038213754	0.006372567	0.04458632
Cr6c10m25a0		1907.7067	611.76403	2519.4707	0.018301879	0.005869053	0.024170932
Cr6c12m25a0		1835.6583	624.80866	2460.467	0.017610672	0.005994199	0.023604871
Cr6c16m25a0		1690.7888	619.42752	2310.2163	0.016220844	0.005942574	0.022163418
c___m25a0		2286.7469	324.9448	2611.6917	0.02193826	0.003117408	0.025055669
Cr6c8m25a6		3516.7265	613.39686	4130.1234	0.03373826	0.005884718	0.039622978
Cr6c10m25a6		3399.0336	606.44588	4005.4795	0.032609155	0.005818032	0.03842787
Cr6c12a6kw	[.994 , .104]	3312.5305	620.32263	3932.8532	0.03177275	0.005951161	0.037730436
Cr6c20m25a6		3109.7162	608.09346	3717.8096	0.029833544	0.005833839	0.035667382
c___m25a6		3990.413	320.78109	4311.194	0.038282644	0.003077463	0.041360108
c___m2a0		1536.5886	248.15394	1784.7425	0.023033595	0.003719849	0.026753444
Cr6c8m2a6		2688.5502	436.54474	3125.0949	0.040301599	0.006543843	0.046845442
Cr6c10m2a6		2609.8792	415.67439	3025.5535	0.039122313	0.006230995	0.045353308
Cr6c12m2a6		2549.2683	425.12118	2974.3895	0.038213752	0.006372603	0.044586355
Cr6c20m2a6		2416.4477	425.35887	2841.8066	0.03622759	0.006376166	0.042598925
c___m2a6		3114.3046	244.90537	3359.2099	0.046683693	0.003671153	0.050354846
Cr6c8m15a6		2089.9049	286.21153	2376.1164	0.055693962	0.007627263	0.063321225
Cr6c10m15a6		2036.5519	280.33807	2316.89	0.054272157	0.007470741	0.061742898
Cr6c12m15a6		1994.3705	280.5279	2274.8984	0.053148061	0.0074758	0.060623861
Cr6c20m15a6		1905.8042	282.13247	2187.9366	0.050787854	0.00751856	0.058306414
c___m15a6		2396.8636	171.07026	2567.9339	0.063874118	0.004558859	0.068432977
Cr6c8m3a6	Error in adapt NAN						
Cr6c10m3a6		4271.0537	781.00809	5052.0618	0.028454872	0.005203279	0.033658151
Cr6c12m3a6		4158.3072	809.36821	4967.6754	0.027703725	0.005392217	0.033095947
Cr6c20m3a6		3911.0865	810.14464	4721.2311	0.026056676	0.005397395	0.031454071
c___m3a6		4985.7181	397.56364	5383.2818	0.033216152	0.002648673	0.035864825
Cr6c8m125a6		1972.3695	217.29982	2189.6694	0.075688932	0.008338798	0.08402773
Cr6c10m125a6		1953.7793	215.18282	2168.9621	0.07497554	0.008257559	0.083233099
Cr6c12m125a6		1919.3273	212.33729	2131.6646	0.073653457	0.008148363	0.081801819
Cr6c125m3a6		1855.2574	211.65367	2066.9111	0.071194799	0.008122129	0.079316928
c___m125a6							
cr6c8_20_Str		3344.0826	664.16621	4008.2488	0.032081975	0.006371781	0.038453756
cr6c8_20_1kink		3344.59494	671.54692	4016.0963	0.032086452	0.006442589	0.038529042
cr6c8_20_2kink		3332.6749	672.42129	4005.0963	0.031972532	0.000645098	0.038423511
cr0c8_20_str	Limit 2refine	2937.2471	690.21636	3627.7635	0.028181813	0.00066217	0.034803511
cr0c8_20_str	Limit 3refine	2974.4943	683.71226	3631.2065	0.028277243	0.006559299	0.034836542
Cr0c114m15a6		1946.27	305.35595	2251.6259	0.051866229	0.008137443	0.060003697
Cr0c114m2a6		2276.3391	475.78639	2752.1255	0.034122518	0.007132079	0.041259
Cr0c114m25a6		2728.7242	730.71954	3459.4437	0.026178438	0.007010271	0.0331887
Cr0c12m15a6		1910.3745	313.12301	2223.4975	0.050909649	0.008344282	0.059254078
Cr0c12m2a6		2210.5116	502.68151	2713.1932	0.03313576	0.007535239	0.040670999
Cr0c12m25a6		2616.1056	777.54241	3393.648	0.025098014	0.000745947	0.032557

	LiftData (N/m^2)						
CaseName	Pressure	Viscous	Total	Pressure	Viscous	Total	L/D
Airfoilkwdone	3091.9	-2.92098	3089.0683	0.029663478	-2.8023E-05	0.029635455	0.246
br6c8_1tan	1942.5516	-2.07882	1940.4937	0.01863617	-1.97E-005	0.018616427	0.174
Naca 66-206	452.17808	0.14716309	452.32524	0.15949423	5.19E-005	0.15954614	20.579
Cr6c8m25a0	-1478.1145	4.9374946	-1473.177	-0.01418052	4.74E-005	-0.014133152	-0.558
Cr6c12m25a3	6989.4034	-27.367422	6962.036	0.067053924	-0.002625536	0.06679137	2.536
Cr6c12m3a0	-2155.51	7.0943161	-2148.4157	-0.014360569	4.73E-005	-0.014313305	-0.645
Cr6c12m2a0	-1068.41	3.3304515	-1065.0795	-0.01601558	4.99E-005	-0.015965634	-0.628
naca_m3a0	-1904.7057	5.2893701	-1899.4163	-0.012689645	5.24E-005	-0.012654406	-0.546
Cr6c12m2a6	13529.219	-41.258553	13487.961	0.20280416	-0.006184693	0.20218569	4.535
Cr6c10m25a0	-1512.349	5.0552861	-1507.2937	-0.014508954	4.85E-005	-0.014460456	-0.598
Cr6c12m25a0	-1546.478	5.0960735	-1541.3819	-0.014836376	4.89E-005	-0.014787486	-0.626
Cr6c16m25a0	-1641.425	5.3349414	-1636.0901	-0.015747265	5.12E-005	-0.015696083	-0.708
c____m25a0	-1226.5949	3.2734791	-1223.3214	-0.011767528	3.14E-005	-0.011736123	-0.468
Cr6c8m25a6	16034.525	-59.206579	15975.318	0.1538297	-0.000568007	0.15326169	3.868
Cr6c10m25a6	15832.003	-58.185727	15773.817	0.15186677	-0.000558214	0.15132855	3.938
Cr6c12a6kw	15637.44	-59.533	15577.9	0.1500202	-0.005711434	0.14944905	3.961
Cr6c20m25a6	15140.517	-57.983047	15082.534	0.1452529	-0.005562693	0.14469663	4.057
c____m25a6	17804.67	-29.549061	17775.121	0.17081186	-0.000283483	0.17052838	4.123
c____m2a0	-931.51367	-24.304576	-955.81825	-0.01396347	-0.003643277	-0.014327798	-0.536
Cr6c8m2a6	13858.755	-42.325884	13816.429	0.20774392	-0.000634469	0.20710946	4.421
Cr6c10m2a6	13699.744	-40.249351	13659.495	0.20536034	-0.000603341	0.204757	4.515
Cr6c12m2a6	13529.224	-41.259121	13487.965	0.20280424	-0.000618478	0.20218576	4.535
Cr6c20m2a6	13144.201	-41.054003	13103.147	0.1970327	-0.00615403	0.1964173	4.611
c____m2a6	15297.695	-23.051042	15274.644	0.22931376	-0.000345537	0.22896822	4.547
Cr6c8m15a6	12468.644	-27.862012	12440.782	0.33227741	-0.000742496	0.33153491	5.236
Cr6c10m15a6	12327.394	-27.312914	12300.08	0.32851324	-0.000727863	0.32778537	5.309
Cr6c12m15a6	12206.601	-27.420834	12179.18	0.3252942	-0.000730739	0.32456346	5.354
Cr6c20m15a6	11886.353	-27.279406	11859.073	0.31675991	-0.00072697	0.31603294	5.420
c____m15a6	13463.561	-16.278326	13447.283	0.358791	-0.004338018	0.3583572	5.237
Cr6c8m3a6							
Cr6c10m3a6	18073.281	-74.878786	17998.402	0.1204089	-0.000498862	0.1191004	3.563
Cr6c12m3a6	17848.786	-77.287427	17771.499	0.11891326	-0.00514909	0.11839835	3.577
Cr6c20m3a6	17299.247	-77.213939	17222.033	0.11525209	-0.000514419	0.11473767	3.648
c____m3a6	20576.969	-36.04203	20540.927	0.13708913	-0.002401214	0.13684901	3.816
Cr6c8m125a6	13124.805	-20.969637	13103.836	0.50365942	-0.000804702	0.50285472	5.984
Cr6c10m125a6	13162.795	-20.885492	13141.91	0.50511726	-0.000801473	0.50431579	6.059
Cr6c12m125a6	13037.133	-20.54474	13016.589	0.50029504	-0.000788397	0.49950665	6.106
Cr6c125m3a6	12785.769	-20.403816	12765.365	0.49064902	-0.000782989	0.48986603	6.176
c____m125a6							#DIV/0!
cr6c8_20_Str	15466.312	-64.297492	15402.014	0.014837846	-0.000616848	0.14776161	3.843
cr6c8_20_1kink	15479.578	-64.164564	15415.414	0.14850573	-0.000615573	0.14789016	3.838
cr6c8_20_2kink	15472	-65.01803	15407.013	0.1484332	-0.006237605	0.14780956	3.847
cr0c8_20_str	16103.261	-65.954317	16037.307	0.15448913	0.00632743	0.15385639	4.421
cr0c8_20_str	16106.657	-65.385831	16041.272	0.15452171	-0.000627289	0.1538942	4.418
Cr0c114m15a6	12374.846	-29.5454	12345.301	0.32977779	-0.000787357	0.3289901	5.483
Cr0c114m2a6	14066.282	-45.891195	14020.391	0.21085478	-0.000687913	0.2101668	5.094
Cr0c114m25a6	16605.484	-70.064066	16535.42	0.15930728	-0.00067217	0.1586351	4.780
Cr0c12m15a6	12290.245	-30.328177	12259.917	0.32752324	-0.000808217	0.32671502	5.514
Cr0c12m2a6	13964.125	-48.449013	13915.676	0.20932343	-0.000726255	0.20859718	5.129
Cr0c12m25a6	16481.321	-74.672858	16406.648	0.15811611	-0.000716386	0.15739	4.835

APPENDIX B

Structural Analysis Data

Stress Peaks (MPa)

Channel Height	Type	Reinforced?	Tapered Flange?	Maximum Stress
0	.75c Spar			3.18E+08
0	.15c Spar			3.17E+08
12	circle			3.21E+08
12	circle			3.23E+08
12	circle	Yes		3.18E+08
12	square			3.26E+08
12	slot 50	Yes		3.29E+08
12	slot 50			3.50E+08
12	square	Yes		3.21E+08
12	slot			3.30E+08
12	slot	Yes		3.22E+08
12	slot 25			3.42E+08
12	slot 25	Yes		3.27E+08
8	circle			3.17E+08
8	circle	Yes		3.17E+08
10	circle			3.20E+08
10	circle	Yes		3.17E+08
16.6	circle			3.34E+08
16.6	circle	Yes		3.25E+08
12	slot 50	Yes	Yes (#1)	3.30E+08
12	slot 50	Yes	Yes (#2)	3.20E+08
12	slot 25		Yes (#2)	3.20E+08
12	slot 25	Yes	Yes (#1)	3.22E+08
10	slot 50	Yes	Yes (#1)	3.27E+08
10	slot 50			3.27E+08
10	slot 50	Yes	Yes (#3)	3.18E+08
11.4	slot 50	Yes	Yes (#5)	3.18E+08

Taper Dimensions

Taper #	Mid-Spar (.382m) Dimension	Change at each end +/- (m)
1	0.021504	0.005589
2	0.021504	0.004391
3	0.021504	0.003498
5	0.021504	0.004128